

Balloon Measurements of Cosmic Ray Muon Spectra in the Atmosphere along with those of Primary Protons and Helium Nuclei over Mid-Latitude

R. Bellotti, F. Cafagna, M. Circella* and C. N. De Marzo
*Dipartimento di Fisica dell'Università di Bari and INFN-Sezione di Bari,
Via Amendola 173, 70126 Bari, Italy*

R. L. Golden† and S. J. Stochaj
*Particle Astrophysics Laboratory, New Mexico State University,
Las Cruces, New Mexico 88003*

M. P. De Pascale, A. Morselli and P. Picozza
*Dipartimento di Fisica dell'Università di Roma "Tor Vergata" and INFN-Sezione di Roma II,
Via Carnevale 15, 00173 Rome, Italy*

S. A. Stephens
Tata Institute of Fundamental Research, Bombay 400 005, India.

M. Hof, W. Menn and M. Simon
Universität Siegen, 57068 Siegen, Germany

J. W. Mitchell, J. F. Ormes and R. E. Streitmatter
NASA Goddard Space Flight Center, Greenbelt, Maryland 20771

N. Finetti, C. Grimani‡, P. Papini§, S. Piccardi and P. Spillantini
*Dipartimento di Fisica dell'Università di Firenze and INFN-Sezione di Firenze,
Largo Enrico Fermi 2, 50125 Florence, Italy*

G. Basini and M. Ricci
INFN Laboratori Nazionali di Frascati, Via Enrico Fermi 40, 00044 Frascati, Italy
(March 6, 1999)
(To appear in Phys. Rev. D)

We report here the measurements of the energy spectra of atmospheric muons and of the parent cosmic ray primary proton and helium nuclei in a single experiment. These were carried out using the MASS superconducting spectrometer in a balloon flight experiment in 1991. The relevance of these results to the atmospheric neutrino anomaly is emphasized. In particular, this approach allows uncertainties caused by the level of solar modulation, the geomagnetic cut-off of the primaries and possible experimental systematics to be decoupled in the comparison of calculated fluxes of muons to measured muon fluxes. The muon observations cover the momentum and depth ranges of 0.3–40 GeV/c and 5–886 g/cm², respectively. A comparison of these results with those obtained in a previous experiment by the same collaboration using a similar apparatus allows us to search for differences due to the different experimental conditions at low energy and to check for the overall normalization between the two measurements. The proton and helium primary measurements cover the rigidity range from 3 to 100 GV, in which both the solar modulation and the geomagnetic cut-off affect the energy spectra at low energies. From the observed low-energy helium spectrum, the geomagnetic transmission function at mid-latitude has been determined.

*Electronic address: circella@ba.infn.it

†Deceased.

‡Also at Dipartimento di Fisica dell'Università di Urbino, Urbino, Italy.

§Electronic address: papini@fi.infn.it

I. INTRODUCTION

Data on muon spectrum as a function of the atmospheric depth in the momentum interval 0.3–40 GeV/ c have been published earlier by this collaboration [1]. We report in this paper a new measurement of muon spectra in the atmosphere as well as the spectra of proton and helium nuclei which were measured at the float altitude with the same apparatus during the same balloon flight. The measurements were performed with the MASS (Matter Antimatter Spectrometer System) apparatus on September 23, 1991 starting from Ft. Sumner, NM at 1270 m above sea-level. The coordinates of this location are 34°N and 104°W, corresponding to an effective vertical cut-off rigidity of about 4.3 GV. The balloon ascent lasted for almost 3 hours, during which about 240,000 triggers were collected. The muon measurements cover the altitude range from ground level to 36 km, which corresponds to about 5 g/cm² of atmospheric depth. The ascent curve of the apparatus, based on the pressure measurements taken by the payload sensors is shown in Fig. 1. The float data analyzed for this work cover an exposure time of about 10 hours. These data were taken at atmospheric depths between 4 and 7 g/cm², with an average value of 5.8 g/cm².

Primary cosmic ray particles, while entering the Earth atmosphere, interact with the atmospheric nuclei and produce secondary particles (see [2], for an excellent introduction). Among the primary cosmic rays, protons and helium nuclei are the major components, and as a consequence, a large fraction of these secondary particles are produced by them. Most of the secondary particles decay and some of the decay products are muons and neutrinos. Muons and muon neutrinos are the decay products of mesons, and both muon and electron neutrinos are the result of muon decays. Both these kinds of neutrinos are detected by underground detectors.

Due to this close relationship, atmospheric muons have been often considered as a powerful tool to calibrate the calculations of atmospheric propagation, in particular for the neutrino flux evaluation (e.g., [3,4]). This situation appears to be most interesting in the context of the increasing evidence of the atmospheric neutrino anomaly (for a recent discussion, see [5]). The anomaly is based on the discrepancy between the observed ratio of the number of neutrino interactions due to μ -type and that due to e -type, as measured by some underground detectors, [6–11] and the robust theoretical expectation at low energy. While the evidence for the anomaly will not be discussed here, it is important to note that any interpretation of the phenomenon depends crucially on the absolute value of the expected fluxes of neutrinos.

In order to take into account the details of particle propagation and interactions in the calculations of atmospheric cascades, both analytic [12–14] and Monte Carlo approaches [15–17] have been successfully undertaken in the past. An extensive work has investigated the differences between the recent neutrino calculations [18], indicating that the parametrization of the cross-sections for meson creation in proton collisions with the atmospheric nuclei is one of the major reasons for this discrepancy. It is well known that at low transverse momentum p_T the perturbative quark model does not work and, moreover, the data available from accelerator measurements are not enough to discriminate between different interaction models in the central collision region (Feynman $x_L \leq 0.1$). Contribution from this experimentally unexplored region is important for the meson production. An additional factor of inaccuracy may come from the kinematics of the particle propagation and decay. Although these processes are well known, their description in the atmospheric simulation codes requires some approximations. In fact, most of the calculations published so far are performed under the approximation of unidimensional propagation of the secondaries, and the effect of this approximation on the low-energy neutrino results is still under study.

Another important input to the atmospheric propagation calculations, which may introduce a further degree of uncertainty, is the primary cosmic ray composition and flux. The direct measurements of the primary components show sometimes significant discrepancies with respect to one another (see [19], for a compilation). The differences in the experimental results are to some extent due to the specific conditions of the measurements, namely, the geomagnetic suppression and the solar modulation, and in part may be due to experimental inaccuracies. Both the geomagnetic and solar cycle effects on the primary cosmic rays need to be taken into account to evaluate the neutrino fluxes, since the underground experiments collect events coming from a large interval of geomagnetic locations over significant fractions of the solar activity cycles. While the geomagnetic suppression is a well understood mechanism and significant improvements in its description have been introduced recently [20], the solar modulation of cosmic rays is not exactly periodic and shows some peculiarities (e.g., the so-called “Forbush events”) that are hard to describe in a model.

A comparison of the expected muon fluxes to measurements of muons in the atmosphere may help in reducing the uncertainty in the neutrino calculations due to the above factors, namely the primary spectra and the interaction cross-sections; both affect to similar extent the muon and neutrino flux calculations. An obvious limitation to this approach is that the muon measurements are not always available in experiments, by which primary particle spectra are measured, and calculations are carried out using available primary spectra measured at a time and location, which may not correspond to the muon measurements. The approach described in this investigation to measure the primary spectra of protons and helium nuclei along with the measurement of atmospheric muons by the same experiment, allows

the following possibilities. (i) The measured primary spectra can be used as input to the propagation calculations whose results have to be compared to the muon measurements, thus taking automatically into account the specific levels of geomagnetic suppression and solar modulation of the experiment. (ii) Possible systematics on the global normalization of the experiment (e.g., geometric factor, acquisition efficiency, etc.) will be compensated as well in such calculations.

While muon measurements at sea-level are widely reported in the literature, there have been very few attempts to measure the muon flux as a function of altitude. The early experiments were performed either with airplane-borne apparatus or at mountain sites [21,22]. Counter telescopes were used for detecting charged particles and muons were usually selected by requiring them to traverse large amounts of matter without interacting. The main difficulty in such experiments was to properly identify muons while rejecting the other components of the “hard” radiation. This problem was of course more complex for positive muon measurements, since the proton flux rapidly increases with increasing altitude. A thorough review of these earlier results is presented in [23]. The deployment of balloon-borne detectors allows the investigation to be extended to momentum and depth ranges much larger than in previous experiments [1,24–26].

Preliminary results for the muon measurements from this study were reported earlier [27,28], as well as preliminary proton results at float level [29]. The measurement of the muon flux and charge ratio at the float level from this experiment has already been published [30].

II. DETECTOR SETUP

The apparatus used in the 1991 experiment was a modified version of the MASS spectrometer flown by the same collaboration in 1989 [31]. It consisted of a superconducting magnet spectrometer, a time of flight device (T.O.F.), a gas threshold Cherenkov detector and an imaging calorimeter, as shown in Fig. 2.

The magnet spectrometer consisted of the NMSU single coil superconducting magnet and of a hybrid tracking device. The magnet, with 11,161 turns and a current of 120 A, gave rise to a field strength of 0.1–2 T in the region of the tracking device. The latter consisted of three groups of multiwire proportional chambers interleaved with two drift chambers, for a total height of 110 cm. Each drift chamber was equipped with ten sensitive layers, each with 16 independent cells. The drift tubes were filled with CO₂. The multiwire proportional chambers were filled with “magic gas”, and were read by means of the cathode-coupled delay line technique [32]. A total number of 19 measurements along the direction of maximum curvature and 8 measurements along the perpendicular direction were performed. The maximum detectable rigidity for this configuration of the spectrometer was estimated to be about 210 GV for singly charged particles [33].

The time of flight detector consisted of two planes of scintillator separated by a distance of 2.36 m. The upper plane was located at the top of the apparatus. It consisted of two layers of scintillator, segmented into 5 paddles of 20 cm width and variable length in order to match the round section of the payload’s shell. The bottom plane, consisting of a single scintillator layer segmented into two paddles, was located below the tracker system and above the calorimeter. A coincidence between the signals from the two planes produced the trigger for data acquisition. The signals from each paddle of scintillator were independently digitized for time of flight measurements as well as for pulse height analyses.

The Cherenkov detector consisted of a 1 m tall cylinder of Freon 22 at the pressure of 1 atm. A four-segment spherical mirror focussed the light onto four photomultipliers. The threshold Lorentz factor for Cherenkov emission was $\gamma_{th} \approx 25$.

The calorimeter consisted of 40 layers, each having 64 brass streamer tubes. Tubes from adjacent layers were arranged perpendicular to one another. The total depth of the calorimeter was 40 cm, equivalent to 7.3 radiation lengths and 0.7 interaction lengths for protons.

III. DATA ANALYSIS

The general features of the data analysis procedures were the same for the three studies illustrated here. Nevertheless, we used different sets of criteria for selecting different particles, due to the different kinds of background events to be eliminated and the extent of the rigidity over which the analysis was carried out in each of these cases. Additional difficulties for the ascent analysis arise because of the possible shocks during the launch and of the rapidly changing environmental conditions with altitude, namely, atmospheric pressure and temperature. We accurately monitored the instrumental conditions continuously during the ascent in order to make sure that the detector performances did not change significantly during the data acquisition. Further, in the case of the ascent analysis, the relative intensity of

different particles change with altitude, and this might mimic instrumental drifts. Because of these reasons, we used a stringent selection for ascent muons, in such a way to make use of the full information recorded for each event. A great deal of effort was put into checking the consistency of the ascent selection with the muon analysis at float, which has been illustrated separately [30].

The proton and helium events from the float file were identified by selecting charge 1 and 2 particles by means of the scintillator signals. The selection of muon events from the ascent file were mainly obtained by identifying singly charged particles which did not interact in the calorimeter. The track reconstruction in the spectrometer allowed the sign of charge of the particles to be determined. Low-energy muons were discriminated from protons by means of the time of flight measurement. Details of the event selection and analyses are described in the following sections.

A. Event Reconstruction

The criteria imposed for the selection of good reconstructed tracks were based on the experience gained with this spectrometer in this and in other flights [33–35]. Although the spectrometer had some multiple track capabilities, only single track events were selected for analysis. The criteria used for the reconstruction of events in the spectrometer are summarized in Table I. This set of criteria was sufficient to select clean good events for the track reconstruction from both the ascent and the float samples. Among the tests shown in this Table, Tests 1–6 were introduced in order to select only good quality reconstructed tracks. In addition, the required consistency between the track extrapolation to the scintillator plane and the position obtained from the scintillator information (Test 7), the requirement that the extrapolated track pass through the calorimeter (Tests 8) and the rejection of tracks intersecting the lift bar of the payload (Tests 9) removed multiple tracks and events generated in interactions in the payload. Finally, Test 10 on the particle velocity as determined with the time of flight measurement rejected albedo events.

B. Proton and Helium Selection

The identification of protons and helium events in the float sample was performed by analyzing the pulse heights of the two independent signals, I_1 and I_2 , from the top layers of scintillator.

The selection for charge 1 particles (protons) was:

$$0.7I_0 < \frac{I_1 + I_2}{2} < 1.8I_0, \quad (3.1)$$

where I_0 is the mean signal from a singly charged minimum ionizing particle. The selection for charge 2 particles (helium) was:

$$3.5I_0 < \frac{I_1 + I_2}{2} < 6I_0. \quad (3.2)$$

Such selection criteria are illustrated in Fig. 3. The lower cut in the helium selection, as given by the above equation, is necessary in order to reduce the proton contamination in the helium sample. For the same reason, consistency between the amplitudes of the two signals I_1 and I_2 was also required for helium selection:

$$\frac{|I_1 - I_2|}{\sqrt{2}} < 0.4 * I_0. \quad (3.3)$$

These selection criteria are appropriate for rigidities above a few GV, relevant to this work. The results concerning the proton and deuterium components in the atmosphere below the geomagnetic cut-off will be presented separately (see [29] for a preliminary report).

C. Muon Selection

The criteria for the identification of muons of either charge are shown in Table II. The scintillator selection (Test 1) for identifying singly charged particles was the same as for the float protons (3.1). For the muon selection, the number of hits detected in the calorimeter was counted separately for each view, in order to account for the different streamer tube efficiency. Both the minimum number of signals and the number of multiple hits refer to the hits contained in a cylinder of radius of 5 streamer tubes along the track extrapolation in the calorimeter, corresponding to about 3

Molière radii. In particular, Test 4 is a powerful means of rejecting electrons [37]. An event identified as a negative muon by means of such selection is shown in Fig. 4.

The Cherenkov signal and the time of flight information were used for background rejection. Test 5 was imposed to remove the low-energy electrons and positrons misidentified in the calorimeter. Test 6 rejects low-energy protons from the positive muon sample by a test of the squared mass m^2 which, once the charge Ze is known, can be estimated from the magnetic deflection η and the velocity β as:

$$m^2 = \frac{\frac{1}{\beta^2} - 1}{\eta^2} \times \frac{Z^2 e^2}{c^2}. \quad (3.4)$$

No time of flight test was required below 0.65 GV, since low-energy protons are efficiently rejected by the scintillator pulse height discrimination.

D. Background Estimates and Corrections

1. Proton and Helium Analysis

Protons are the main component of primary cosmic rays. As a consequence, the possible background from light particles, namely, positrons, muons and pions, is expected to be small above the geomagnetic cut-off and is not customarily subtracted from the measurement. Therefore, no correction for such background events has been performed on the proton measurements in this investigation. The contamination from helium events in the selected proton sample is negligible. Further, no attempt was made to separate the isotopes of protons and helium events, even at low energies. In the case of helium selection there could be a small proton contamination due to the Landau fluctuations of the energy released in the scintillator layers from the large flux of protons. This background was evaluated by studying a sample of protons selected by means of the pulse height signals in the bottom scintillator layer. The contamination, in the whole energy range, was found to be less than 2% and for each energy bin the number of the estimated background protons in the helium sample was subtracted.

2. Muon Analysis

The possible sources of background events, which might simulate muon-like events, are listed in Table III. Also shown in this table are the most efficient rejection criteria to eliminate the background events and the estimated levels of residual contamination.

Albedo events are upward-going particles which simulate a curvature of opposite sign in the spectrometer. They are either produced as large angle secondaries in interactions by hadrons incident at large zenith angles or by hard scatterings. However, we found only 9 upward-going events in the whole ascent sample. They were easily removed by means of the time of flight measurement (Test 10 of Table I).

The degree of possible electron contamination varies with altitude and energy because of the different development of the electron and muon fluxes in the atmosphere. For energies $\lesssim 1$ GeV, the worst conditions for the relative ratio of muon to electron flux is expected at less than 100 g/cm², where the muon flux is still increasing with atmospheric depth and the electron flux has already reached its maximum [38]. Low-energy electrons and positrons misidentified as muons in the calorimeter were rejected from the muon sample by means of the Cherenkov selection shown in Test 5 of Table II. We used the number of Cherenkov-identified electron events to estimate the upper limit to the altitude-dependent residual contamination as given in Table III.

Spillover events are particles whose charge sign is misinterpreted in the magnet spectrometer. This source of background needs to be considered for the negative muon sample because of the large number of protons at high altitudes. As a consequence of the high performances of the magnet spectrometer, spillover is expected to be only a negligible source of background in the momentum range of this investigation. In fact, we carried out a simulation [36], which takes into account the details of the magnetic field in the spectrometer and detector response. We found that the spillover background can not be more than 1% of the negative muon events even near the float altitude and at the highest rigidity bin, where one might expect some contribution.

Background due to pions and kaons is the major concern for the muon measurements, because it is not possible to identify mesons that do not interact in the calorimeter. From theoretical expectations for the pion and kaon fluxes in the atmosphere [12,39], we estimated that for muon momenta less than 10 GeV/c pions do not contaminate significantly the muon measurements at depths larger than 200 g/cm², while an altitude-dependent pion contamination of

the order of 1-2% can not be excluded at smaller depths. The fraction of contaminating pions may be larger at larger particle momenta. The kaon contamination is negligible everywhere. There is also the possibility that locally produced particles, namely secondaries produced by hadrons interacting in the shell or in the lift bar above the payload, may be detected as single muon-like events. In order to reject such events, we excluded from the analysis all the tracks whose extrapolation did intersect the lift bar. In addition, we placed severe requirements on the reconstructed tracks, as illustrated previously, by which multiple particles from an interaction that are incident within the instrument can be rejected. From an analysis of simulated events, we estimated that the possible residual contamination from locally produced particles is negligible, except at very low energies and at small atmospheric depths. In order to evaluate the possible extent of contamination in this region, we checked the number of negative events which were selected as muons in the rest of the apparatus and passed a pion selection criterion in the calorimeter. From this fraction and from the estimated efficiency for such a test to detect pions, we estimated that a contamination by locally produced particles at an extent up to 20% can not be excluded for muons below 1 GeV/c at small atmospheric depths. The fraction of such events decreases rapidly with increasing atmospheric depth and we found that it may not exceed 5% at depths larger than 50 g/cm². It should be emphasized that this procedure can allow us only to set the upper limit to the contamination due to this source of background. Therefore no further correction was made to the data. Finally, the proton background is important for the positive muon measurements, since their flux rapidly increases with increasing altitude. Primary protons exponentially attenuate in the atmosphere with an absorption length $\Lambda \sim 120$ g/cm² [2]. This occurrence places a serious constraint on the range of atmospheric depth over which positive muon measurements are possible. However, the situation is different at low energy because of the geomagnetic suppression of primaries, as can be seen from the helium spectrum shown in Fig. 5. The low-energy proton component therefore has to be of a secondary nature. This can also be seen in the altitude distribution of such events [23]. The geomagnetic suppression allows us to perform a low-energy proton rejection by means of the squared mass tests listed in Table II.

E. Geometric Factor and Efficiencies

1. Geometric Factor and Global Efficiencies

The geometric factor of the apparatus was estimated by means of two independent codes for the containment conditions listed in Table I. The accuracy of such calculations was estimated to be better than 1%.

Particles generated at the top of the apparatus were followed down to the bottom of the calorimeter and then traced up to the level of the lift bar. By requiring that the track should not intersect the suspension bar, about 10% of the events above 1 GV that cross the whole detector were eliminated. The deflection dependence of the geometric factor for the different cases is shown in Fig. 6. The small difference between positive and negative particles at high deflection is due to a mechanical asymmetry of the magnet with respect to the detector stack.

The following global efficiencies were introduced in each analysis: (a) a trigger efficiency of 0.825 ± 0.010 measured in a ground test before the launch; (b) a time-dependent livetime fraction, which varied during the ascent as shown in Fig. 7 and reached a value of 0.66 ± 0.01 at float; (c) a rigidity dependent reconstruction efficiency, shown in Fig. 8 for muons. While the reconstruction efficiency, at high energy, is the same for protons and muons, it is significantly lower for helium nuclei. Above the geomagnetic cut-off the reconstruction efficiencies were nearly constant; they were 0.959 ± 0.012 for protons and muons and 0.917 ± 0.032 for helium. No dependence was found on the sign of charge for muons.

2. Proton and Helium Selection Efficiencies

The scintillator efficiencies for charge 1 (protons and muons) and charge 2 (helium) particle selection were determined using samples of events tagged by the bottom scintillator detector; this information was not used in the analysis for the event selection. This technique allows a reliable evaluation of the selection efficiencies. We estimated a selection efficiency of 0.945 ± 0.001 for protons and muons and 0.882 ± 0.022 for helium nuclei.

3. Muon Selection Efficiencies

In addition to the above efficiencies, the following selection efficiencies were considered in estimating the muon fluxes: (a) a calorimeter efficiency of 0.888 ± 0.008 ; (b) the requirement of the presence of the calorimeter information introduced a further efficiency of 0.851 ± 0.005 , because of some acquisition failures; (c) the Cherenkov test at low

energy was passed by muons with an efficiency of 0.998 ± 0.001 ; (d) the efficiency for the time of flight selection of low-energy positive muons was found to be 0.992 ± 0.004 and 0.908 ± 0.014 , respectively in the 0.65–1.25 GV and 1.25–1.5 GV rigidity ranges.

The overall efficiency for muon selection was therefore a function of time and energy. It ranged for negative muons from a minimum of 0.298 ± 0.006 at 0.3 GeV/ c at maximum deadtime to the value of 0.539 ± 0.011 above 4 GeV/ c and at minimum deadtime. The detection efficiency for positive muons was slightly lower because of the additional squared mass selection criterion.

IV. RESULTS

A. Muon Results

With the selection described in the previous sections, we selected a sample of 4,471 negative and 2,856 positive muons distributed in the atmospheric depth range of 5–886 g/cm². As previously mentioned, the momentum range investigated for negative muons was from 0.3 to 40 GeV/ c , while positive muons were selected in the 0.3–1.5 GeV/ c interval.

We followed the same procedure developed for our previous analysis [1] for the reconstruction of the flux growth curves in the atmosphere. In particular, a parametrization of the form:

$$\Phi(X) = kX e^{-X/\Lambda} \quad (4.1)$$

was adopted in order to describe the dependence of the muon flux in the different momentum intervals upon the atmospheric depth X , where k and Λ are varied to fit the data. Results on the depth dependence of muons of either charge are shown in Fig. 9, and are also given in Table IV: it may be noted that the positive and negative curve shapes do not show any noticeable difference.

Fig. 10 shows the muon charge ratio in the atmosphere in two different energy intervals. It can be noticed that our results do not show any definite trend of the charge ratio changing with atmospheric depth. On the other hand, it may be pointed out that the depth-averaged value of the μ^+/μ^- ratio increases with increasing momentum of the particles, being 1.12 ± 0.04 and 1.23 ± 0.05 respectively in the 0.3–0.9 and 0.9–1.5 GeV/ c momentum bins. These values are consistent with the ratio measured at float in the same experiment [30]. Fig. 10 also shows that, while there is a general agreement among results in the low energy bin at large atmospheric depths, there is noticeable difference at low altitudes below 100 g/cm². In addition to the results shown in Fig. 10, results are also available at very small atmospheric depths. The CAPRICE experiment reported an average value of 1.64 ± 0.08 between 0.2 and 2.3 GeV/ c at 3.9 g/cm² of residual atmosphere [40], while a ratio of 1.26 ± 0.12 for 0.3–1.3 GeV/ c muons was previously found at 11 g/cm² [41]. It is not clear from the literature how much of the differences in the observed ratio could be ascribed to the different experimental conditions.

The measured spectra of negative muons at different depths between 25 and 255 g/cm² are shown in Fig. 11 and also in Table V: The results in Table IV show that, in spite of the differences in the growth pattern of the muon flux for different momentum intervals, the estimated value of the effective atmospheric depth (FAD) do not differ by more than 1% at all depths, except at the largest depth interval. Above 1.5 GeV/ c , the negative muon spectra may be parametrized as power-laws with a power index of 2.45 ± 0.05 , almost independent of the atmospheric depth, and in a close agreement with our previous observations in [1]. A comparison between these two measurements shows that the normalizations of the two sets of results are in a good agreement in the 1–8 GeV/ c interval. A comparison between these two experiments at lower energy is less straightforward, due to the different conditions of solar modulation and geomagnetic cut-off of the two experiments. As shown in Fig. 12, we measured a significant deficit of low-energy muons in the 1991 flight with respect to the 1989 experiment over a large range of atmospheric depth.

B. Proton and Helium Results

From the events recorded at the float, we have selected 118,637 proton events and 15,207 helium events for the analysis. These events were collected over a period of 35,330 s. After subtracting the estimated background, the number of events were corrected for the selection efficiencies. The flux for each selected energy bin at the spectrometer level was estimated using the time of observation and the calculated geometric factor. In the case of protons, we have chosen the rigidity range between 3.3 and 100 GV, where the contribution from the atmospheric secondaries is small. The helium spectrum was investigated between 3 and 100 GV.

The estimated flux values at the spectrometer level were corrected to the top of the payload by taking into account inelastic interactions and ionization energy loss in the detectors above the spectrometer (namely, the plastic scintillator counters and the gas Cherenkov detector) and in the aluminum dome of the payload. The proton flux was then extrapolated to the top of the atmosphere by making use of the procedure described by Papini *et al.* [19], which includes the ionization and interaction losses as well as the secondary production in the residual atmosphere above the apparatus. In the case of the helium nuclei, in addition to the ionization and interaction losses, the production by heavy nucleus spallation was taken into account by considering the appropriate helium attenuation length instead of the helium interaction length.

The proton and helium fluxes at the top of the atmosphere are given in Tables VI and VII. The spectral index γ is 2.708 ± 0.037 for protons above 30 GeV and 2.65 ± 0.19 for the helium flux above 15 GeV/n. The measured spectra are shown in Fig. 13, where the geomagnetic effect is evident below 3.5 GeV for protons and below 1.5 GeV/n for helium. The spectral shapes of the data, above the geomagnetic cut-off, show that the solar modulation effect is noticeable despite the high value of geomagnetic cut-off for this experiment.

Because of the penumbral bands associated with the geomagnetic cut-off rigidities at mid-latitudes, primary cosmic rays are partially transmitted through the earth's magnetic field near the cut-off. In the following, we attempt to determine the geomagnetic transmission function, which is defined as the fraction of cosmic rays of given energy to reach the Earth after the interaction with the geomagnetic field, from our observation. For this purpose, we make use of the observed helium spectrum rather than the proton spectrum, because at low energies the secondary production of protons in the atmosphere influences the measured proton spectrum.

In Fig. 14(a) the helium flux is shown as a function of rigidity together with the curve of Fig. 13 corresponding to the maximum of solar modulation [19]. The ratio between the experimental points and the curve is shown in Fig. 14(b). This ratio can be taken as representative of the transmission function. The dashed curve is the best-fit parametrization of the data with a simple curve:

$$GF(R) = \left\{ [(0.920 \pm 0.010) \times (R/R_c)]^{(-23.2 \pm 2.0)} + 1 \right\}^{(-0.385 \pm 0.040)}, \quad (4.2)$$

where $R_c=4.1$ GV represents the average value of the effective vertical cut-off rigidity over the flight trajectory. This average value has been estimated using the vertical cut-off map by Shea and Smart [44]. The position of the payload changed between $34^\circ 43'$ and $35^\circ 29'$ of N-latitude and between $103^\circ 38'$ and $104^\circ 25'$ of W-longitude during the flight, with a small variation in the value of vertical cut-off.

It can be useful to have an analytical representation of the measured primary fluxes. For this purpose, it has been found that a simple function of the form

$$J(E) = a (E + be^{-cE})^{-\gamma} \times GF(E) \quad (4.3)$$

can fit the data both for proton and helium spectra. In (4.3) a , b , c are free parameters, γ is the slope of the spectrum at high energy, $GF(E)$ is the geomagnetic transmission function and E is the kinetic energy per nucleon. The parameter values obtained for protons are: $a = 11169 \pm 121$, $b = 2.682 \pm 0.046$, $c = 0.0950 \pm 0.0059$ with a reduced $\chi^2 = 1.12$; the corresponding values for helium are $a = 406 \pm 14$, $b = 1.416 \pm 0.068$, $c = 0.203 \pm 0.039$ with a reduced $\chi^2 = 0.51$. We found that a parametrization (4.3) can represent, with the same accuracy and in the same energy range explored in this work, the observed spectra of all recent measurements by using different values for the constants.

The comparison of the results from this experiment with data from other experiments is shown in Fig. 15 for protons and in Fig. 16 for helium. In general, it seems that there are several inconsistencies among the different experiments. Such discrepancies cannot be ascribed completely to the solar modulation effect, since they are noticed even at high energies where the solar modulation effect is very small. If we compare only the most recent data, as shown in Fig. 17 for energies above 10 GeV/n, we see that the discrepancies are reduced. However, the differences between different data in some cases are of the order of 20–30%, considerably larger than the estimated errors. It is difficult to establish a priori what systematics affect the different experiments. Therefore, in order to avoid the effect of such systematic errors in the comparison between atmospheric and primary cosmic ray fluxes, the approach proposed in this paper is to use the same apparatus to measure both the atmospheric muons and their parent primary particle fluxes.

V. CONCLUSIONS

We have reported on simultaneous measurements of atmospheric muons and of primary cosmic rays taken with the same apparatus in a balloon experiment. The muon measurements cover the atmospheric depth range between

5 and 886 g/cm². Negative muon spectra were measured in the momentum range 0.3–40 GeV/*c*, while positive muons between 0.3 and 1.5 GeV/*c*. The proton and helium measurements were carried out at 5.8 g/cm², in the 3–100 GV rigidity range. Corrections were applied in order to calculate the expected primary fluxes at the top of the atmosphere. The geomagnetic transmission function at mid-latitude has been determined. The data analysis procedures for primary nuclei and muon fluxes were similar. Nevertheless, some differences in the selection criteria for different particles were used. For this reason we can estimate a normalization uncertainty of 1% between proton and negative muon fluxes, and of 2% between proton and positive muon fluxes. The availability of results of muons and primaries taken with the same detector in the same experiment may help decrease the uncertainties in the atmospheric neutrino calculations.

ACKNOWLEDGMENTS

We acknowledge very useful discussions with T. Stanev, T. K. Gaisser and also with V. A. Naumov. We thank the National Scientific Balloon Facility (Palestine, Texas), which operated the flight. This work was supported by NASA Grant NAG-110, DARA and DFG, Germany, the Istituto Nazionale di Fisica Nucleare, Italy, and the Agenzia Spaziale Italiana, as part of the research activities of the WIZARD collaboration. A special thank to our technical support staff from NMSU and INFN.

-
- [1] R. Bellotti *et al.*, Phys. Rev. D **53**, 35 (1996).
 - [2] T. K. Gaisser, *Cosmic Rays and Particle Physics* (Cambridge University, Cambridge, England, 1990).
 - [3] T. Stanev, Proc. of the IV Int. Workshop on Neutrino Telescopes (M. Baldo Ceolin editor, Venice, Italy, 1992).
 - [4] D. H. Perkins, Nucl. Phys. **B399**, 3 (1993).
 - [5] M. C. Gonzalez-Garcia *et al.*, Phys. Rev. D **58**, 33004 (1998).
 - [6] K. S. Hirata *et al.*, Phys. Lett. B **280**, 146 (1992).
 - [7] R. Becker-Szendy *et al.*, Phys. Rev. D **46**, 3720 (1992).
 - [8] M. C. Goodman *et al.*, Nucl. Phys. B **38**, 337 (1995).
 - [9] Ch. Berger *et al.*, Phys. Lett. B **227**, 489 (1989).
 - [10] M. Aglietta *et al.*, Europhys. Lett. B **8**, 611 (1989).
 - [11] Y. Fukuda *et al.*, Phys. Rev. Lett. **81**, 1562 (1998).
 - [12] A. S. Stephens, Conf. Pap. Int. Cosmic Ray Conf. 17th **4**, 282 (1981).
 - [13] E. V. Bugaev and V. A. Naumov, Phys. Lett. B **232**, 391 (1989).
 - [14] P. Lipari, Astropart. Phys. **1**, 195 (1993).
 - [15] G. Barr, T. K. Gaisser and T. Stanev, Phys. Rev. D **39**, 3532 (1989).
 - [16] M. Honda *et al.*, Phys. Lett. B **248**, 193 (1990).
 - [17] H. Lee and Y. S. Koh, Nuovo Cimento **105B**, 883 (1990).
 - [18] T. K. Gaisser *et al.*, Phys. Rev. D **54**, 5578 (1996).
 - [19] P. Papini, C. Grimani and S. A. Stephens, Nuovo Cimento **19C**, 367 (1996).
 - [20] P. Lipari, T. Stanev and T. K. Gaisser, Phys. Rev. D **58**, 73003 (1998).
 - [21] M. Conversi, Phys. Rev. **79**, 749 (1950).
 - [22] Ya. L. Blokh, L. I. Dorman and I. Ya. Libin, Nuovo Cimento Soc. Ital. Fis. **37B**, 198 (1977).
 - [23] M. Circella, “Muoni nei raggi cosmici. Studio sperimentale dei flussi e del rapporto di carica in atmosfera”, PHD thesis (University of Bari, Italy, 1997), in Italian.
 - [24] J. F. Krizmanic *et al.*, Conf. Pap. Int. Cosmic Ray Conf. 24th **1**, 593 (1995).
 - [25] E. Schneider *et al.*, Conf. Pap. Int. Cosmic Ray Conf. 24th **1**, 690 (1995).
 - [26] S. Coutu *et al.*, “Energy spectra of air shower muons as a function of atmospheric depth”, paper presented at the 29th International Conference on High Energy Physics (Vancouver, 1998). Also in G. Tarlé *et al.*, Conf. Pap. Int. Cosmic Ray Conf. 25th **6**, 321 (1997).
 - [27] G. Basini *et al.*, Conf. Pap. Int. Cosmic Ray Conf. 24th **1**, 585 (1995).
 - [28] G. Basini *et al.*, Conf. Pap. Int. Cosmic Ray Conf. 25th **6**, 381 (1997).
 - [29] P. Papini *et al.*, Conf. Pap. Int. Cosmic Ray Conf. 24th **4**, 1033 (1995).
 - [30] A. Codino *et al.*, J. Phys. G **23**, 1751 (1997).
 - [31] M. P. De Pascale *et al.*, J. Geophys. Res. **98**, 3501 (1993).
 - [32] J. L. Lacy and R. S. Lindsey, Nucl. Instrum. Meth. **119**, 483 (1974).

- [33] M. Hof *et al.*, Ap. J. **467**, L33 (1996).
- [34] M. Hof *et al.*, Nucl. Instr. Meth. A **345**, 561 (1994).
- [35] R. L. Golden, *et al.*, Nucl. Instrum. Meth. A **306**, 366 (1991).
- [36] P. Papini, “Studio e misura degli spettri di antiprotoni e deuterio nei raggi cosmici”, PHD thesis (University of Florence, Italy, 1996), in Italian.
- [37] R. L. Golden *et al.*, Ap. J. **436**, 769 (1994).
- [38] R. R. Daniel and S. A. Stephens, Rev. Geophys. and Sp. Phys. **12**, 233 (1974).
- [39] G. D. Badhwar, S. A. Stephens and R. L. Golden, Phys. Rev. D **15**, 820 (1977).
- [40] G. Barbiellini *et al.*, Conf. Pap. Int. Cosmic Ray Conf. 25th **6**, 317 (1997).
- [41] E. A. Bogomolov *et al.*, Conf. Pap. Int. Cosmic Ray Conf. 16th **1**, 330 (1979).
- [42] I. F. Quercia, B. Rispoli and S. Sciuti, Nuovo Cimento **7**, 277 (1950).
- [43] M. Circella, C. N. De Marzo, T. K. Gaisser and T. Stanev, Conf. Pap. Int. Cosmic Ray Conf. **7**, 117 (1997).
- [44] M. A. Shea and D. F. Smart Conf. Pap. Int. Cosmic Ray Conf. 18th **3**, 411 (1983).
- [45] L. H. Smith, *et al.*, Ap. J. **180**, 987 (1973).
- [46] M. J. Ryan, J. F. Ormes and V. K. Balasubrahmanyam, Phys. Rev. Lett. **28**, 985 (1972).
- [47] E. S. Seo *et al.*, Ap. J. **378**, 763 (1991).
- [48] W. R. Webber, R. L. Golden and S. A. Stephens, Conf. Pap. Int. Cosmic Ray Conf. 20th **1**, 325 (1987).
- [49] J. F. Ormes and W. R. Webber, J. Geophys. Res. **73**, 4231 (1968).
- [50] W. Menn *et al.*, Conf. Pap. Int. Cosmic Ray Conf. 25th **3**, 409 (1997).
- [51] M. Boezio *et al.*, INFN/AE-98/06, Ap. J. (to be published).
- [52] G. M. Mason, Ap. J. **171**, 139 (1972).
- [53] T. T. Von Rosenvinge, F. B. Mc Donald and J. H. Trainor, Conf. Pap. Int. Cosmic Ray Conf. 12th **12**, 170 (1979).
- [54] J. Buckley *et al.*, Ap. J. **429**, 736 (1994).
- [55] J. J. Beatty *et al.*, Ap. J. **413**, 268 (1993).

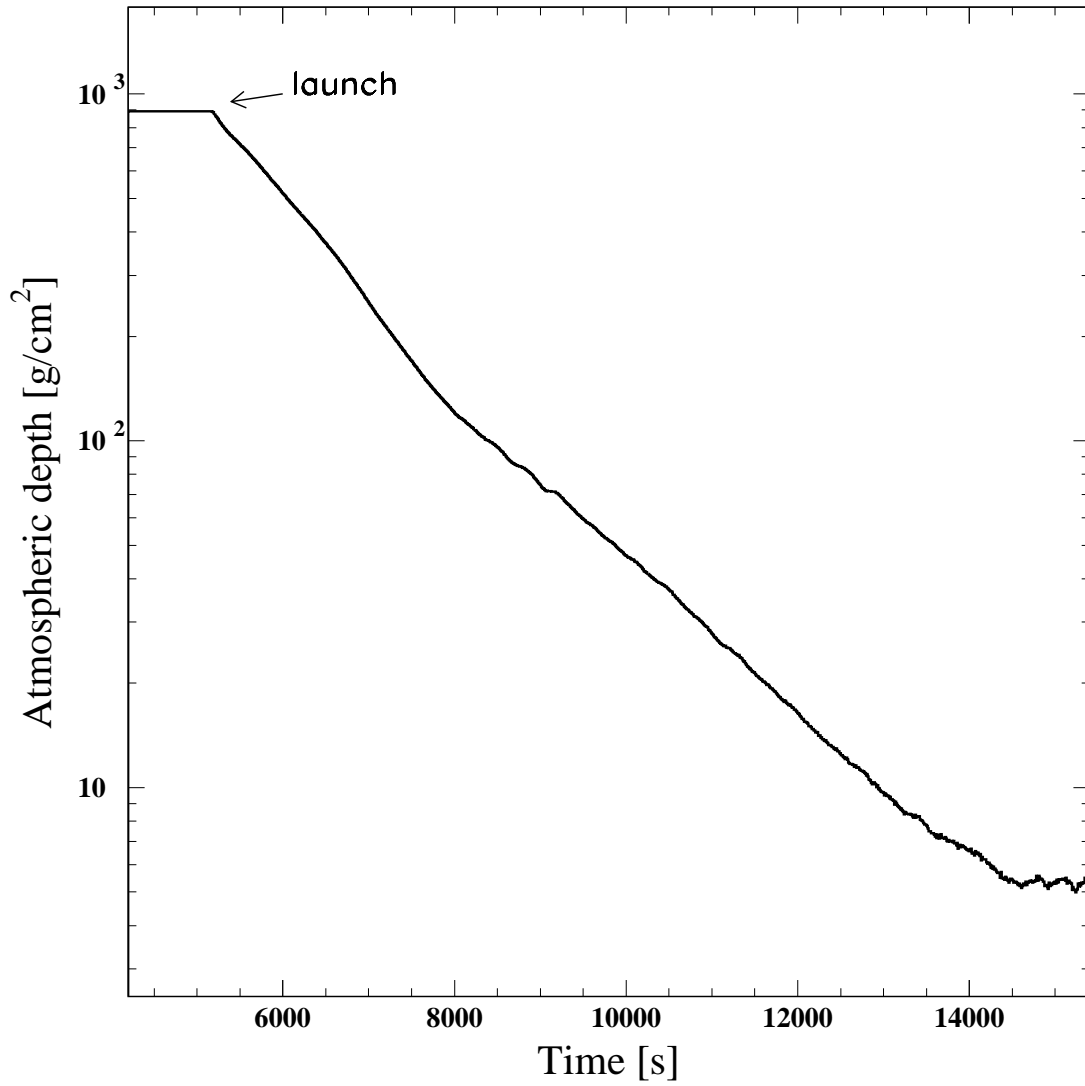


FIG. 1. Ascent curve of the payload, based on the pressure measurements. Time is measured from the startup of the on-board computer and the launch is at 5180 s from this reference time.

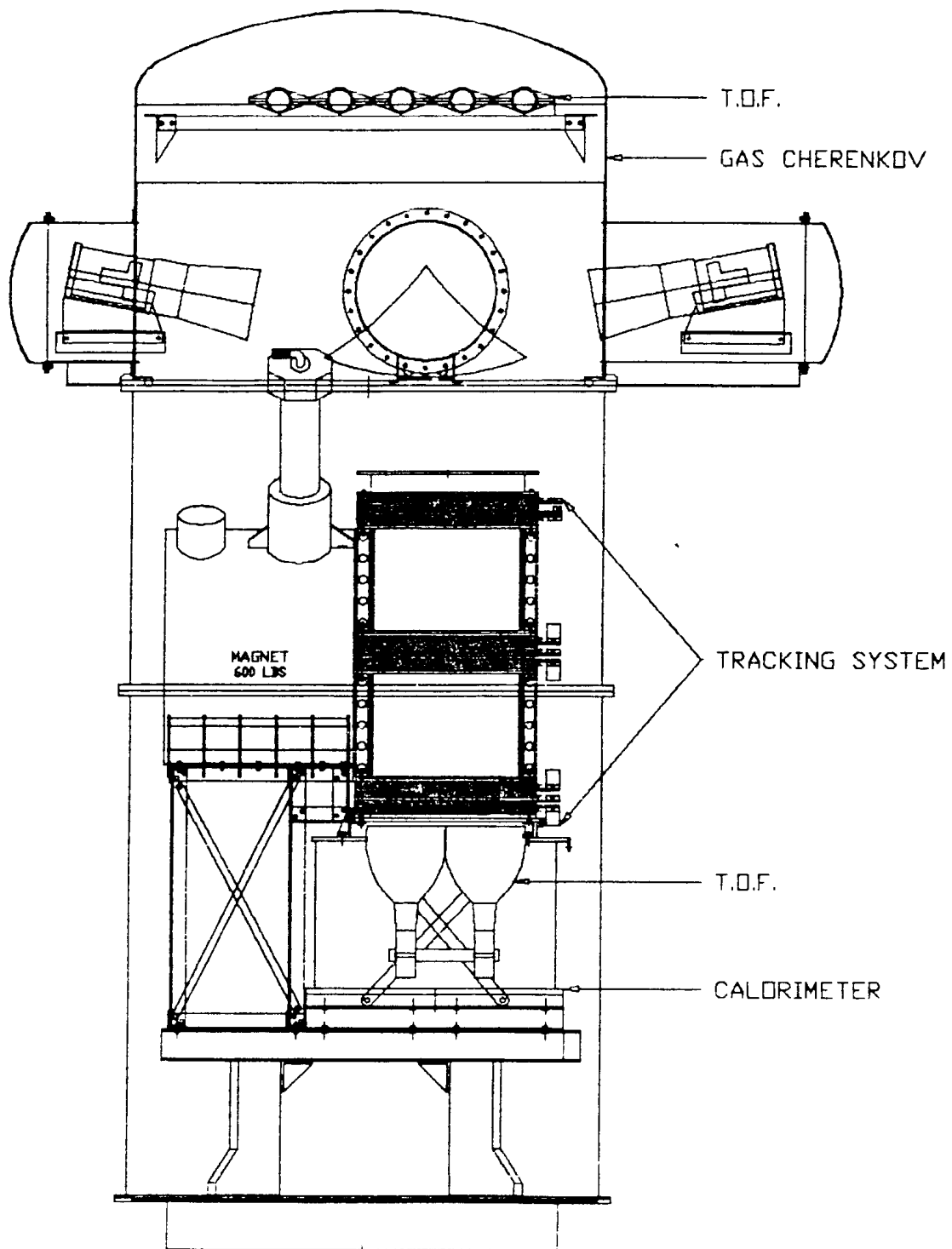


FIG. 2. The MASS apparatus in the 1991 configuration.

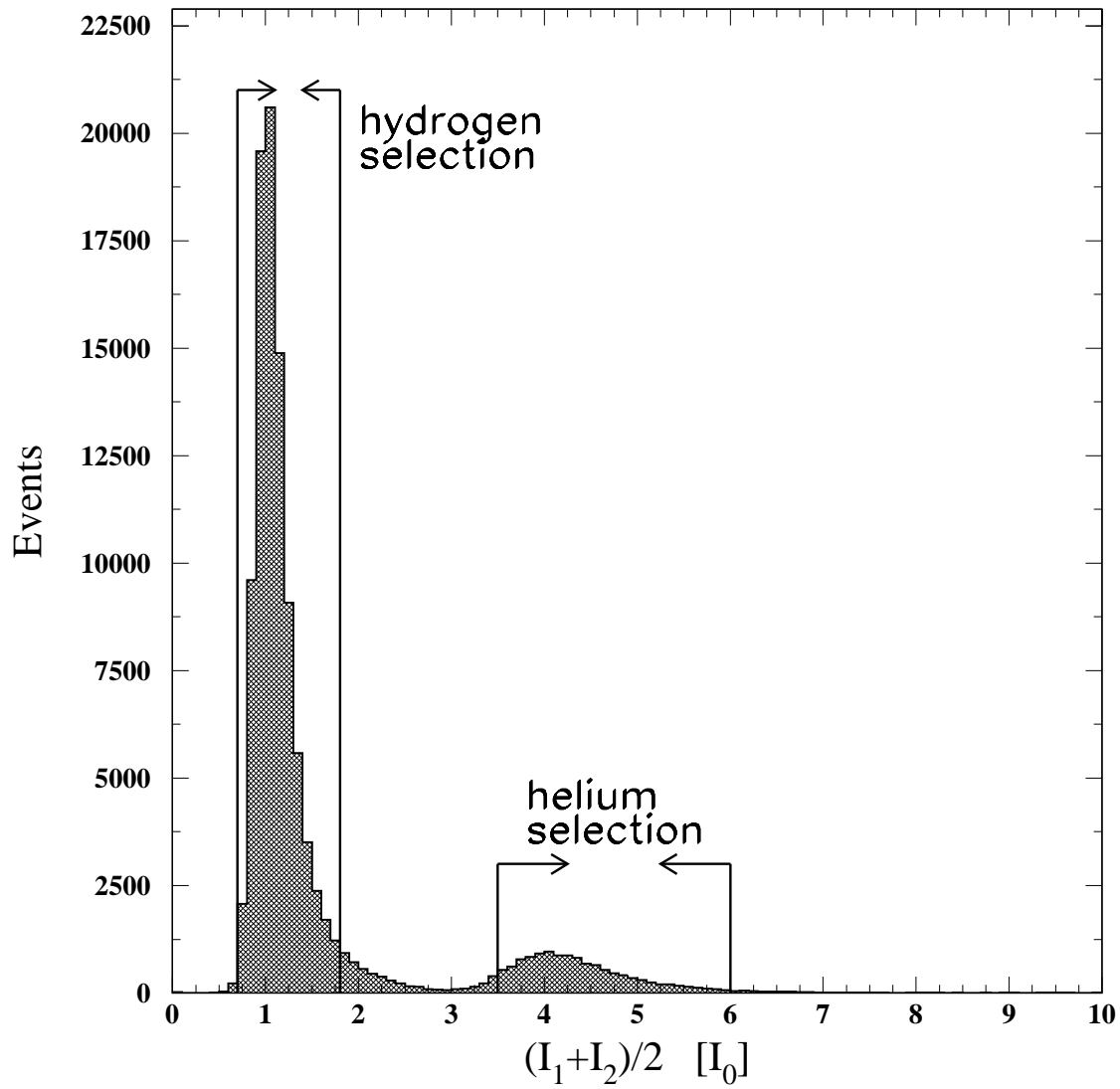


FIG. 3. Distribution of the amplitude signals from the top scintillators for high-energy positive events at float (above 3 GV).

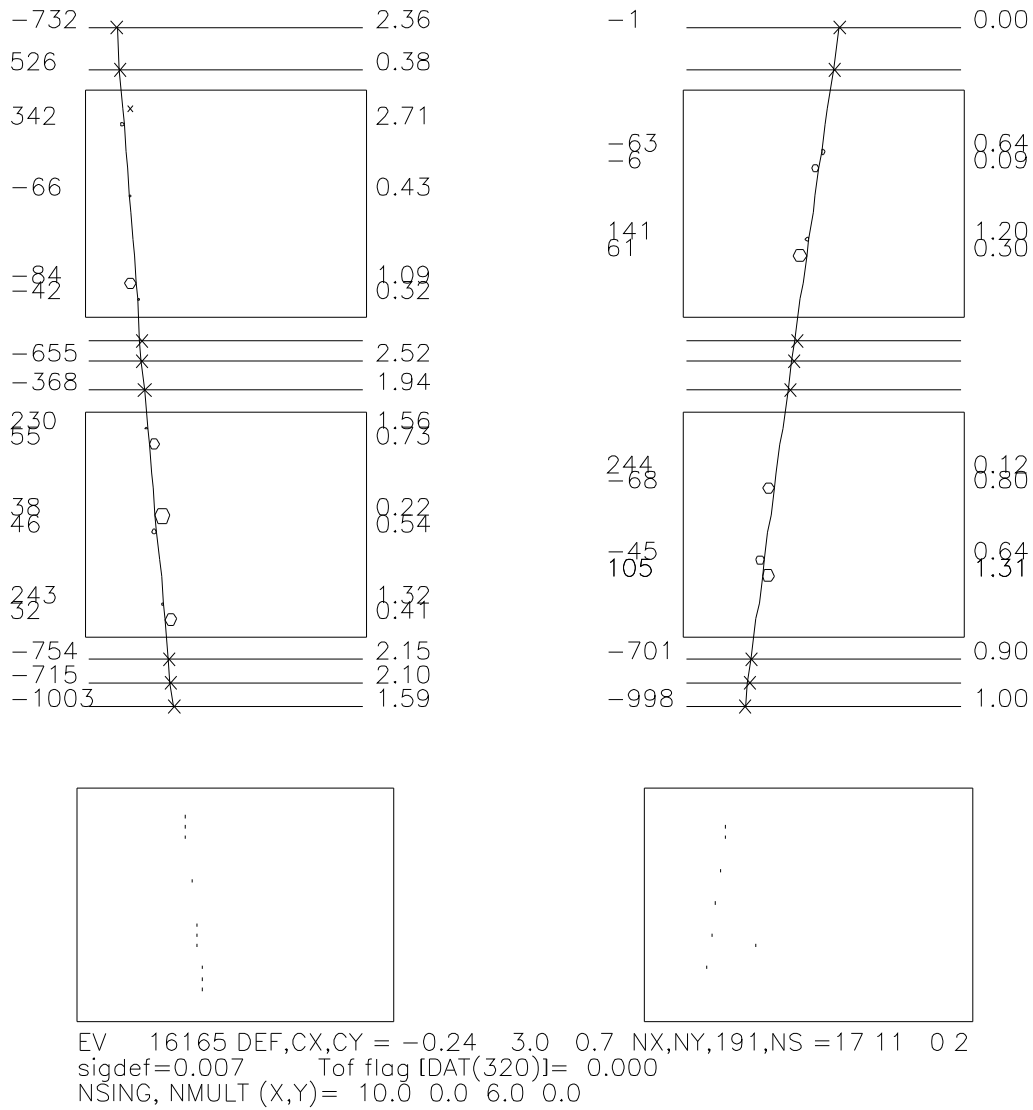


FIG. 4. Negative muon identified in the apparatus. The reconstructed event is shown along the direction of maximum bending in the magnetic field (left) and along the perpendicular view (right). The estimated deflection is $\eta=0.24 \text{ GV}^{-1}$, corresponding to a rigidity $R=4.17 \text{ GV}$. The track in the calorimeter is shown at the bottom.

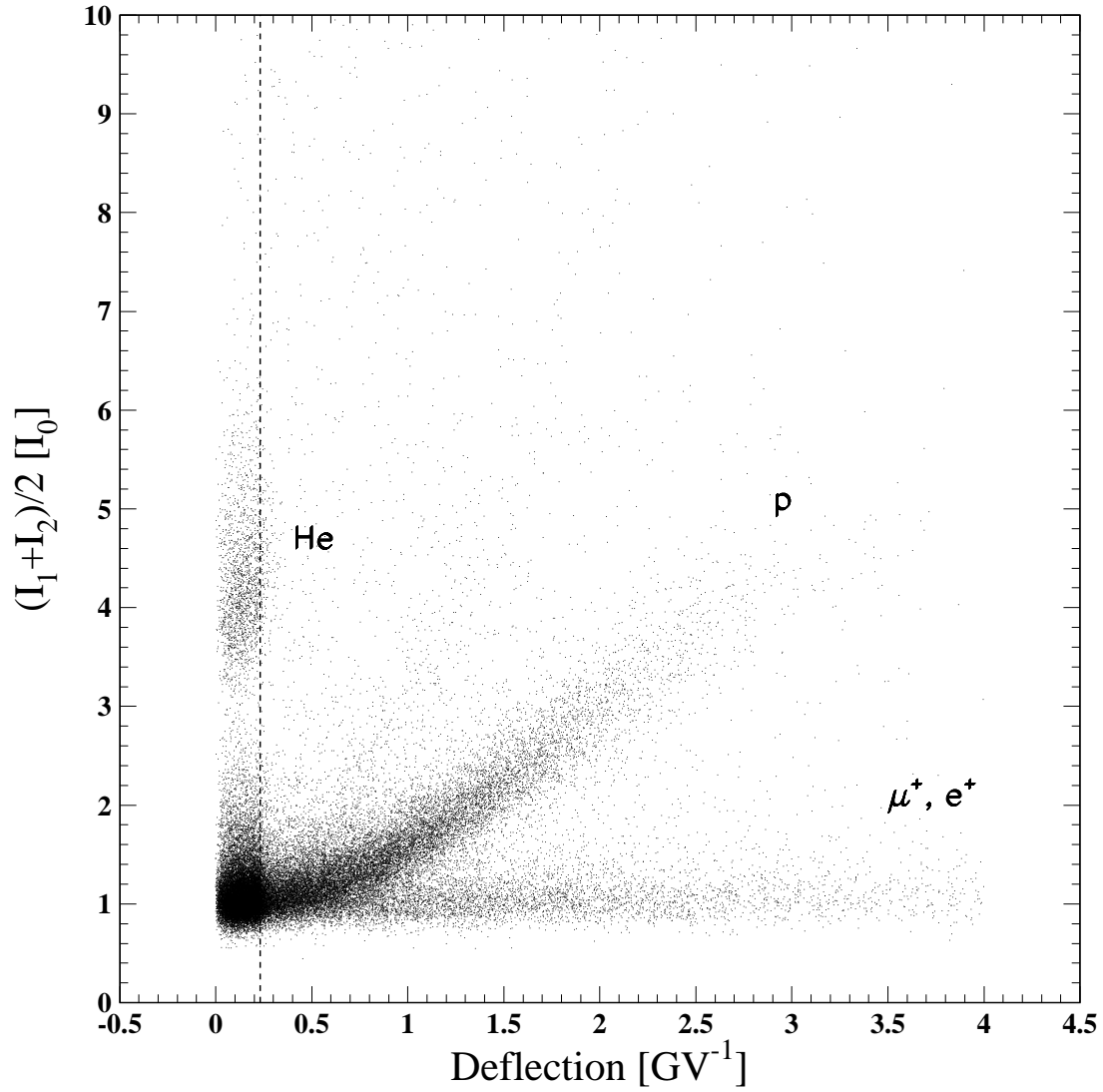


FIG. 5. Mean pulse height in the top scintillators plotted as a function of deflection for the positive particles taken during the ascent. The scintillator signal has been normalized to the average pulse height from singly charged minimum ionizing particles, I_0 . A dashed line shows the value of the vertical geomagnetic cut-off for this experiment. The effect of the cut-off can be seen in the suppression of the low-energy helium component.

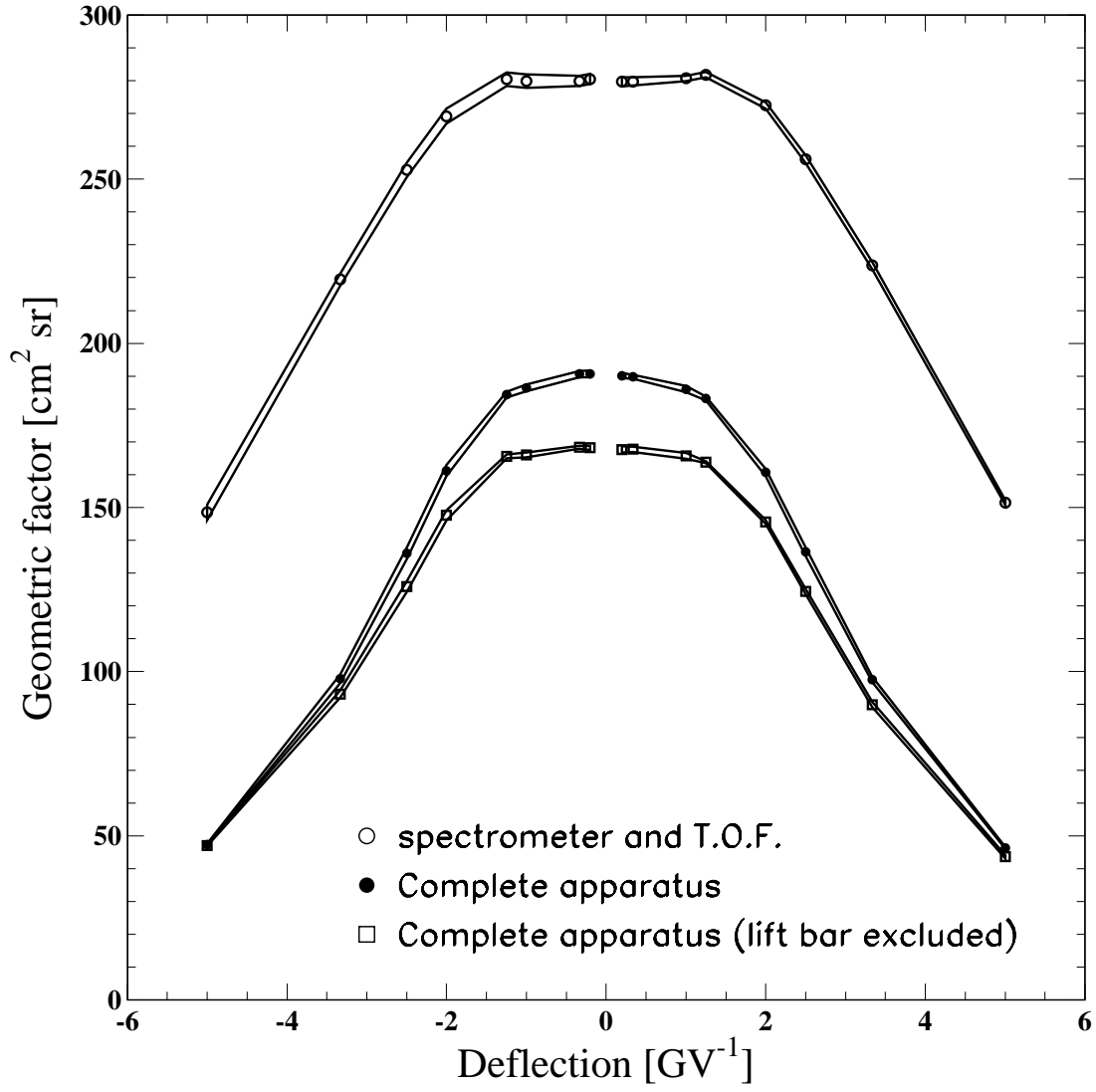


FIG. 6. Geometric factor for different acceptance criteria. The estimated uncertainties are also shown.

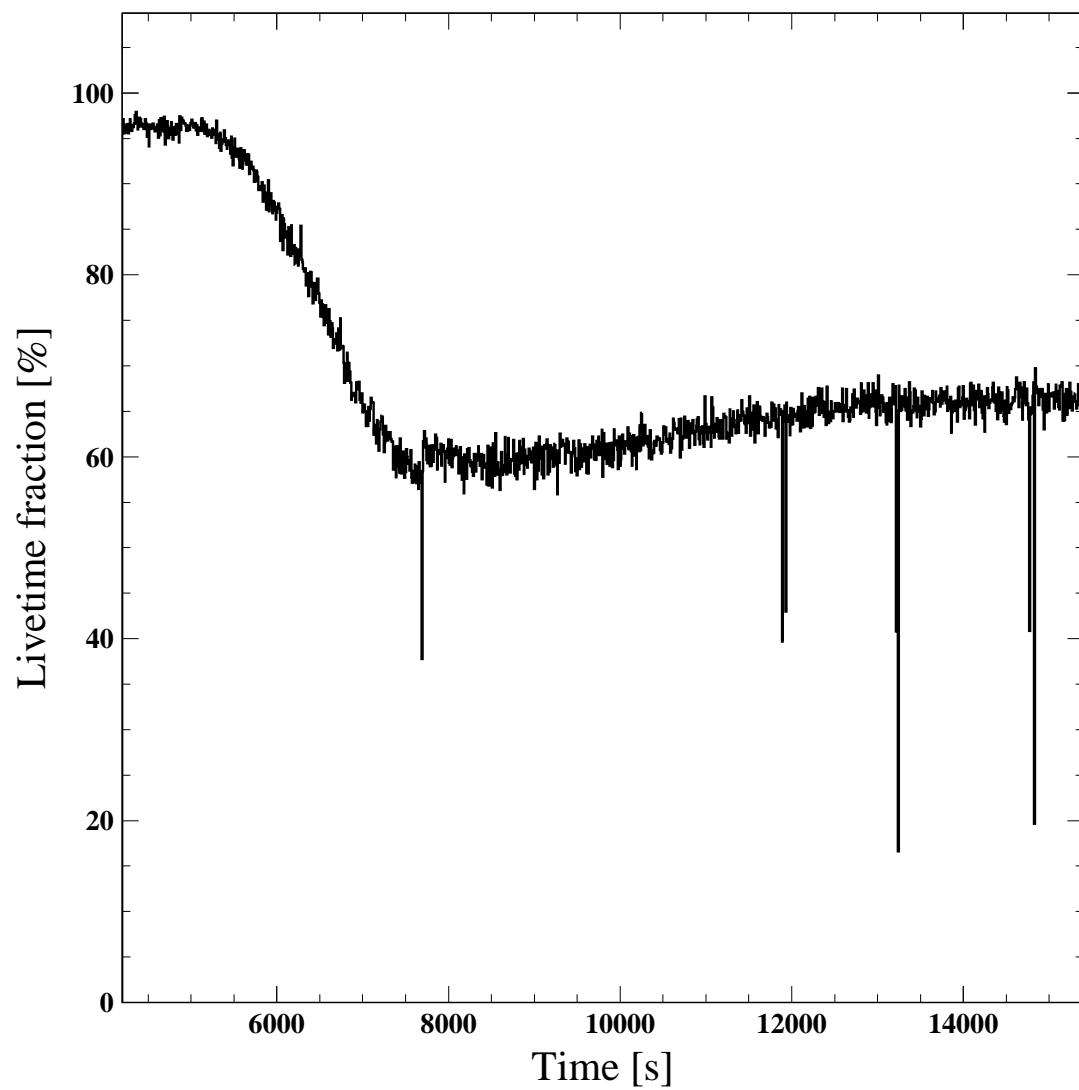


FIG. 7. Livetime fraction during the ascent of the flight.

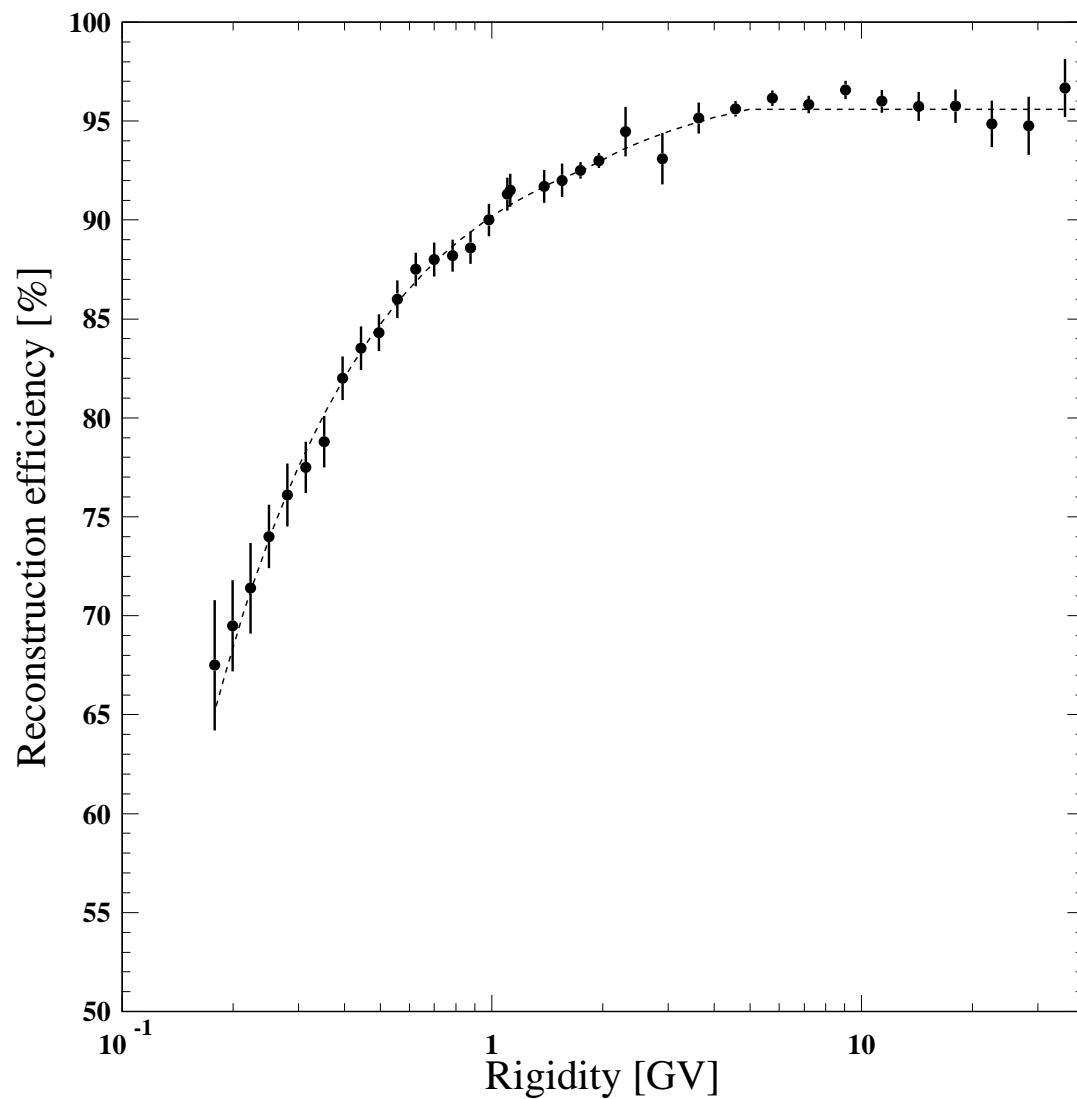


FIG. 8. Spectrometer track reconstruction efficiency for muon particles. The dashed line shows the best-interpolation curve used in the flux calculations.

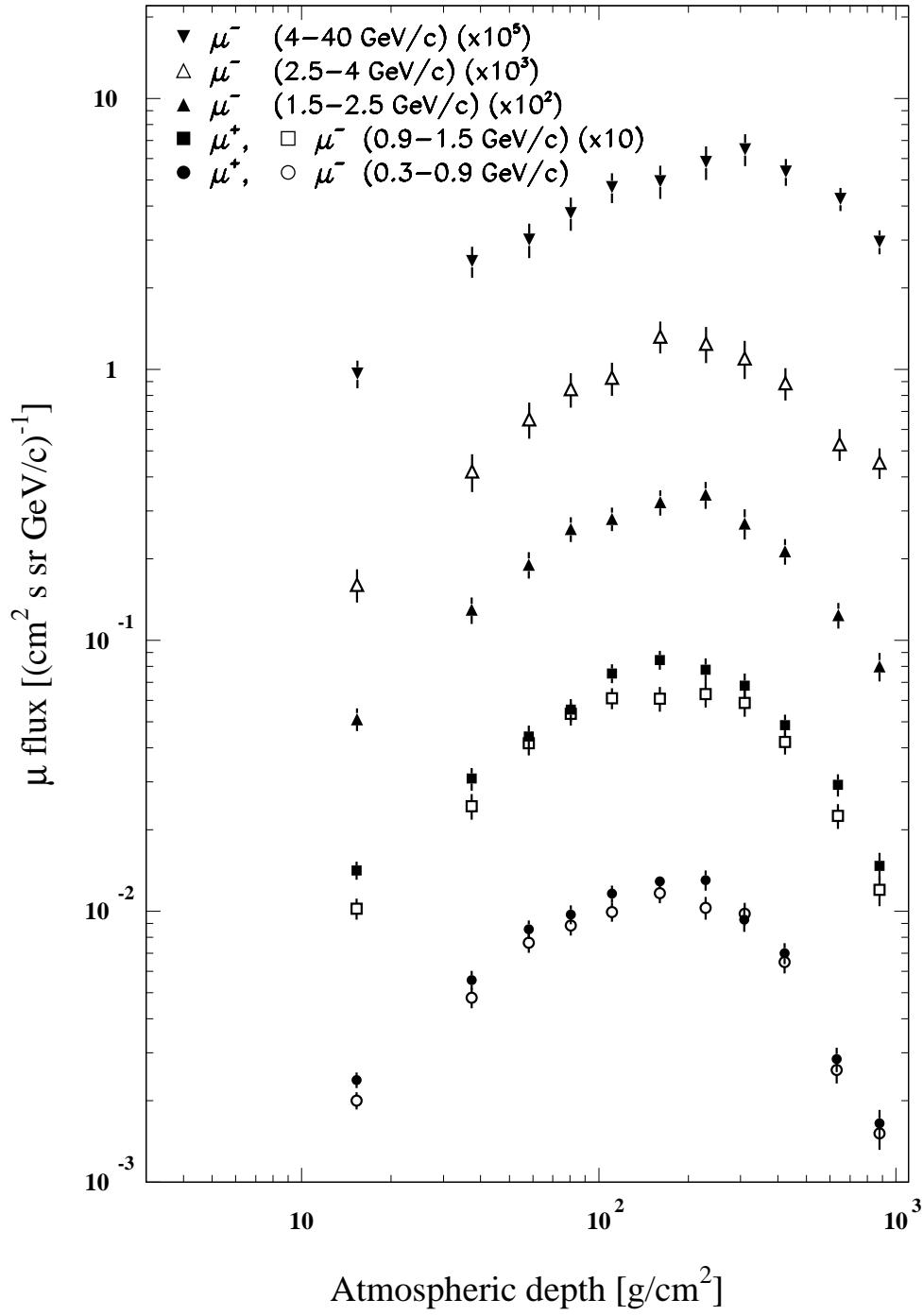


FIG. 9. Flux growth curves for negative muons in the 0.3–40 GeV/c momentum range. Positive muon results are shown in the 0.3–1.5 GeV/c momentum interval. Some of the distributions have been scaled as indicated.

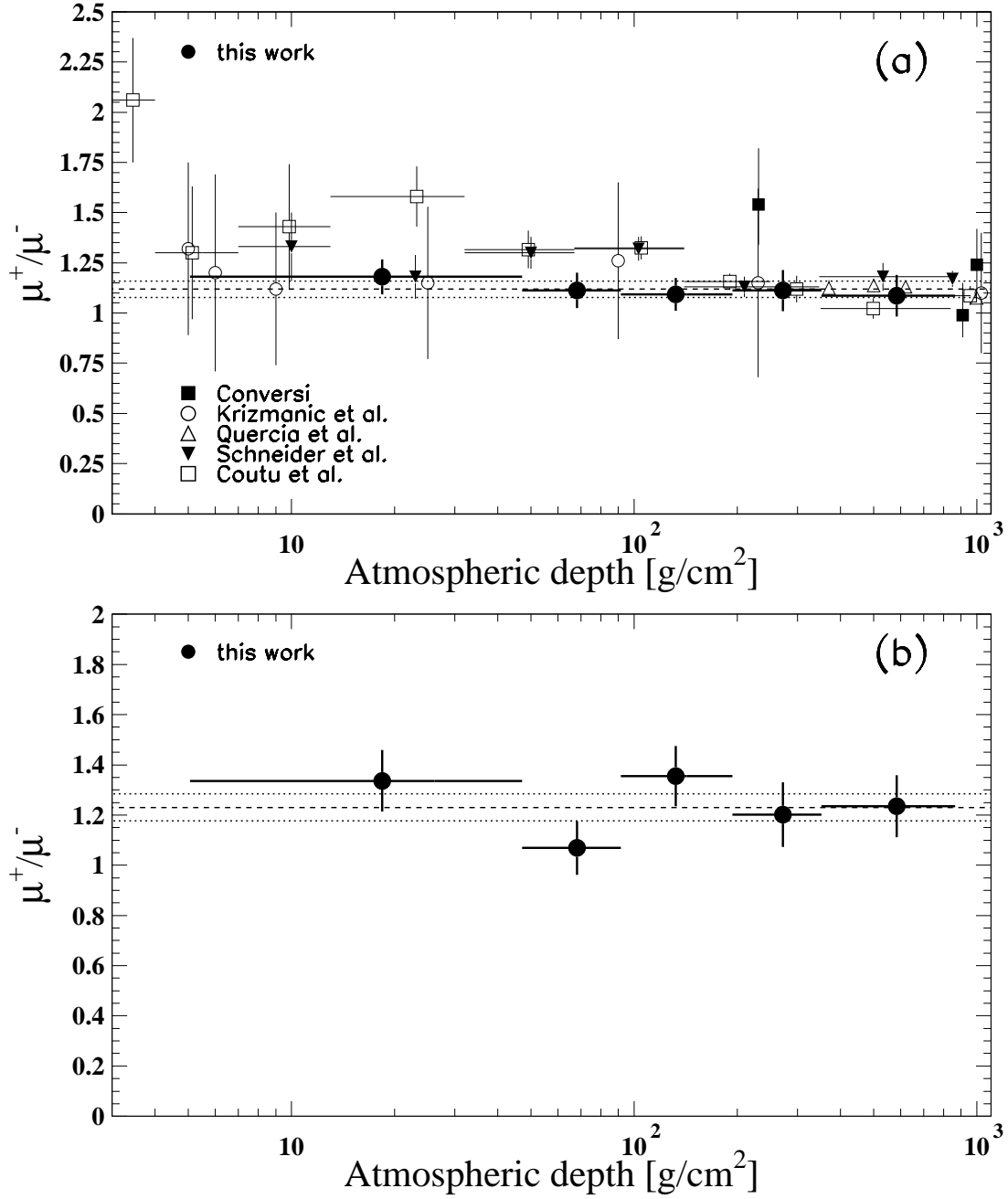


FIG. 10. Muon charge ratio in the (a) 0.3–0.9 GeV/c and (b) 0.9–1.5 GeV/c momentum intervals with changing atmospheric depth. The dashed lines show the weighted average values from this experiment, and the dotted lines the corresponding 1σ intervals. Results from previous experiments are also shown: Conversi (0.315–0.348 GeV/c) [21], Krizmanic *et al.* (0.42–0.47 GeV/c) [24], Quercia *et al.* (≥ 460 MeV) [42], Schneider *et al.* and Coutu *et al.* (0.3–0.9 GeV/c) [25,26].

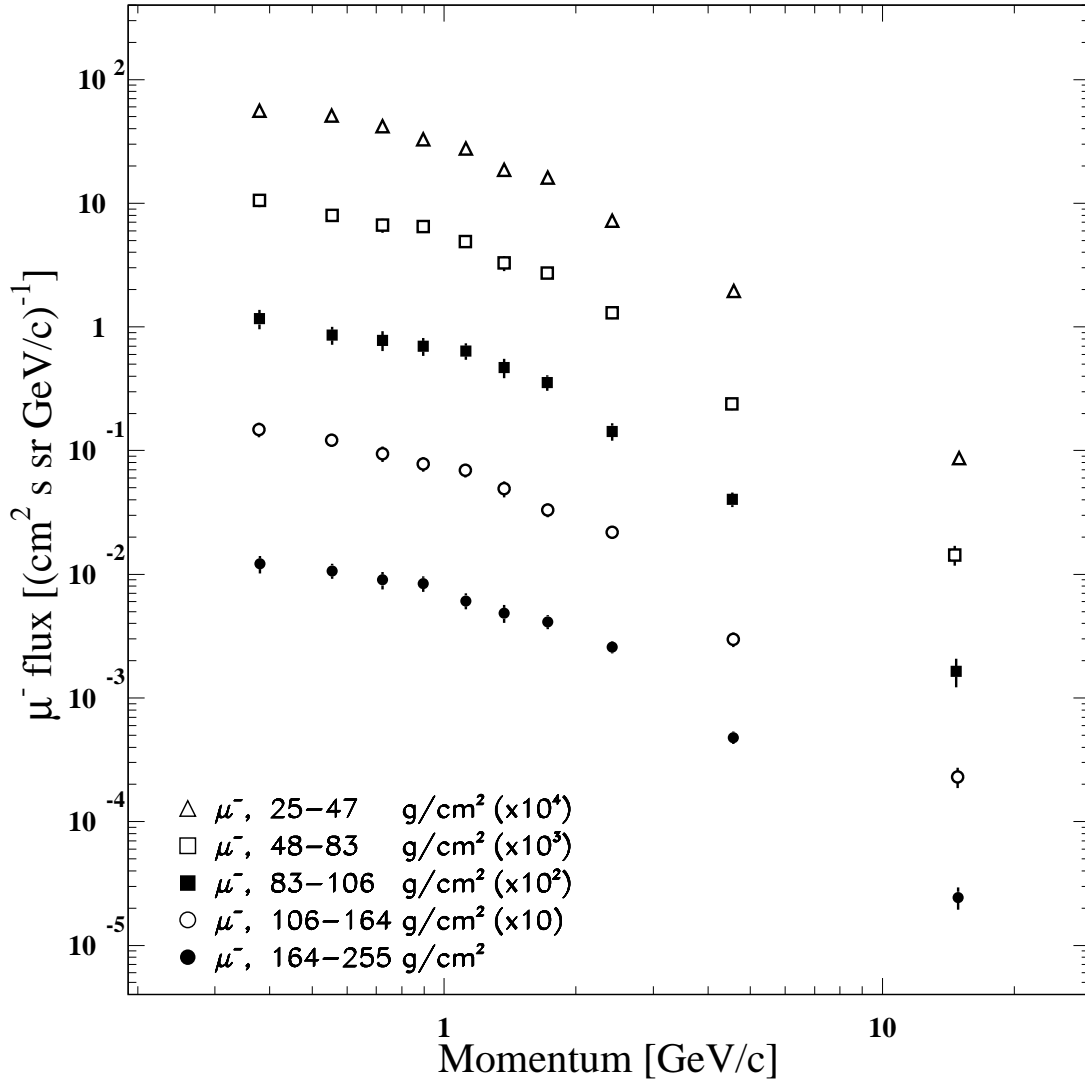


FIG. 11. Negative muon momentum spectra in different depth intervals. Some of the distributions have been scaled as indicated.

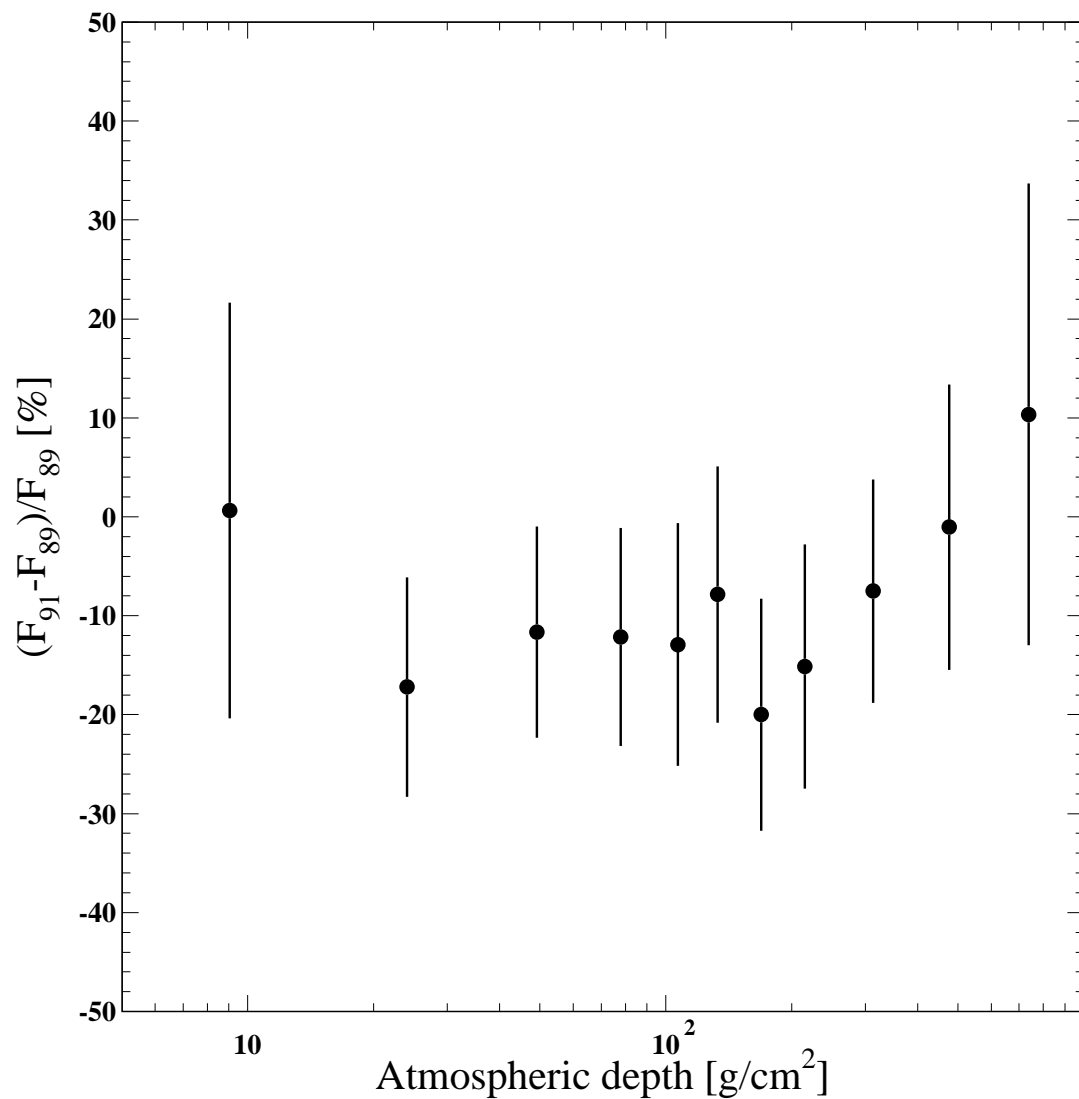


FIG. 12. Differences in the 0.3–1 GeV/ c negative muon flux measured in this experiment with respect to the 1989 experiment [1].

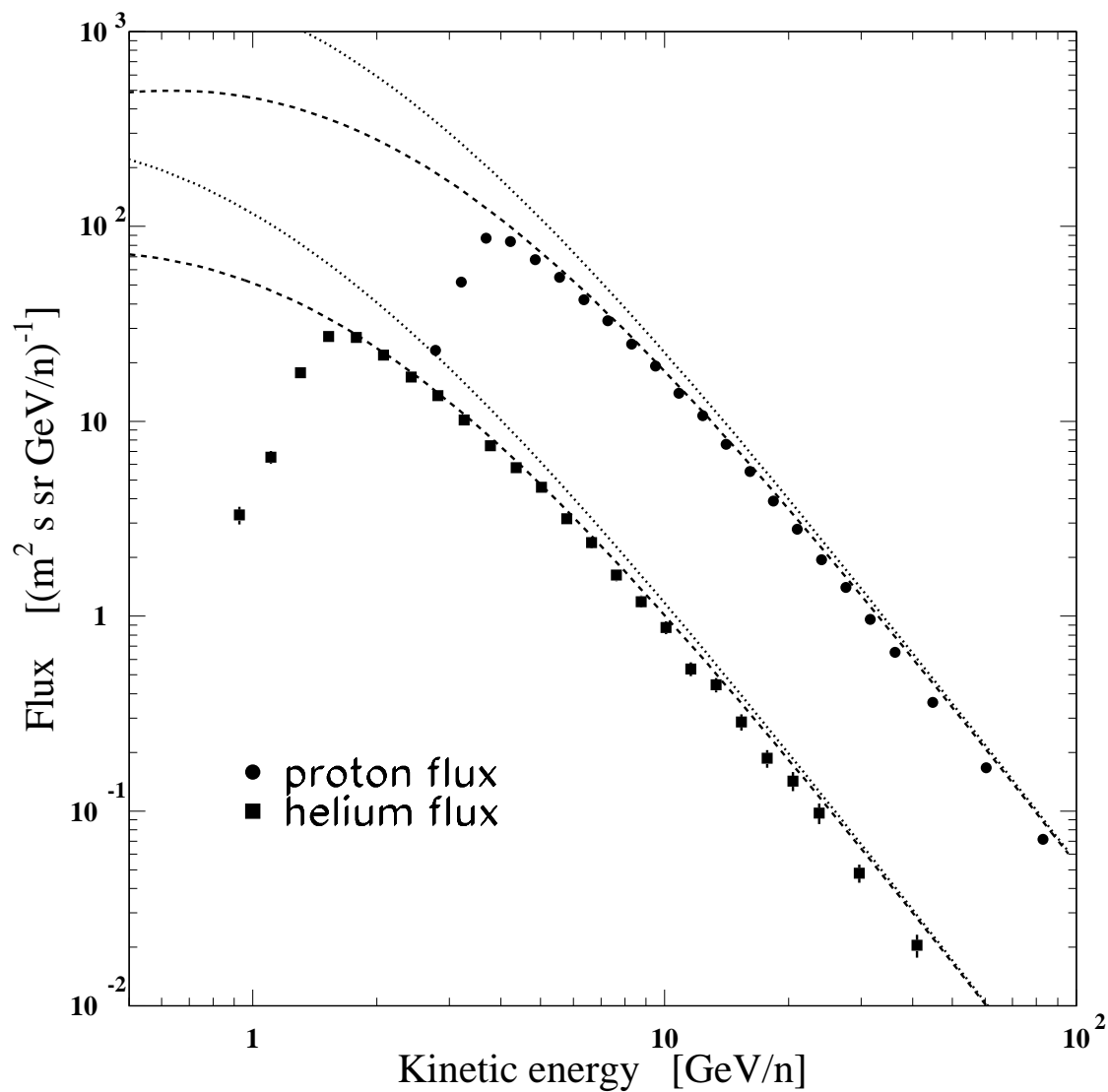


FIG. 13. Proton and helium flux values at the top of the atmosphere are plotted as a function of energy. The superimposed curves represent fits of a previous compilation of data [19] for minimum (dotted) and maximum (dashed) of solar modulation.

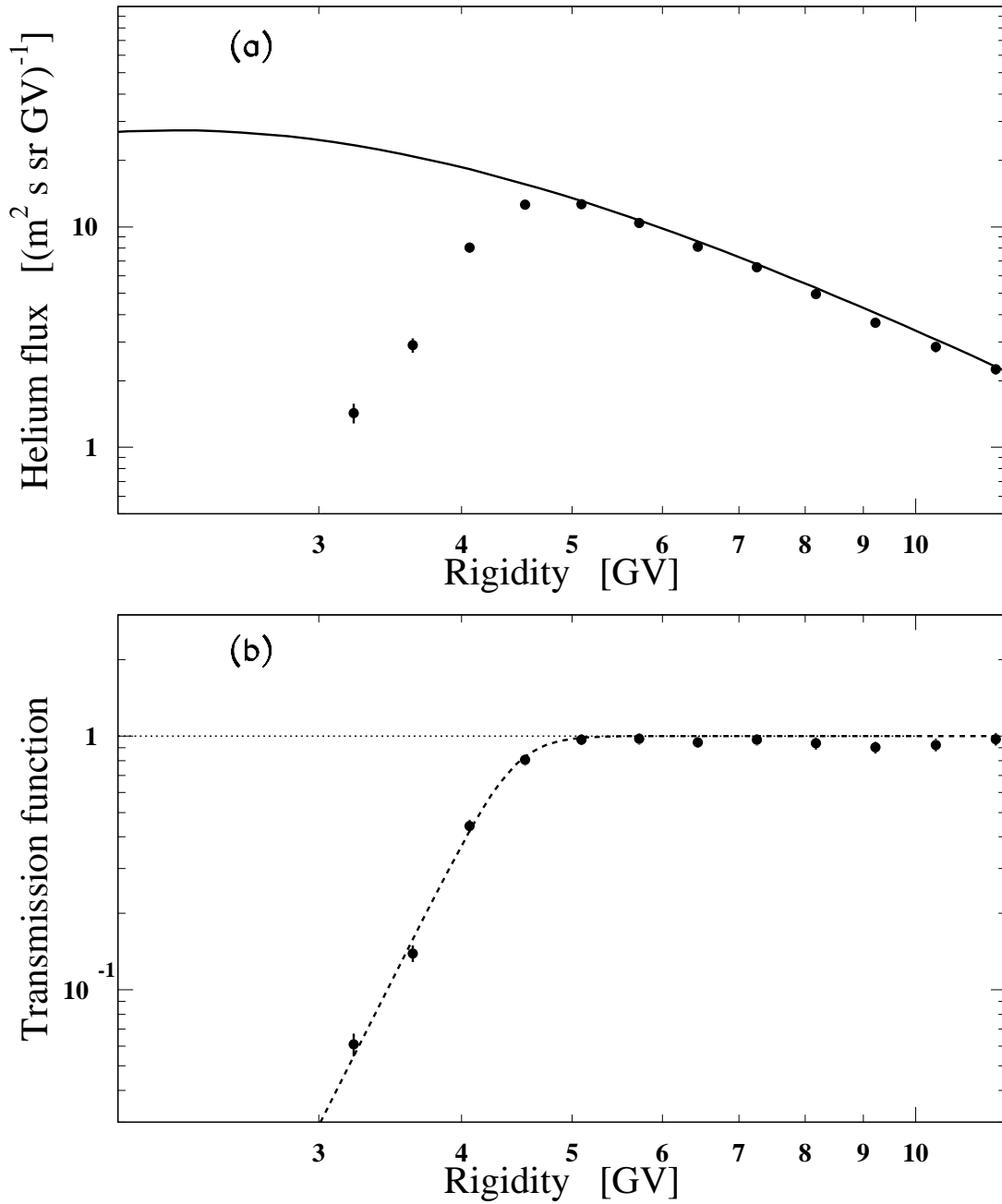


FIG. 14. Transmission function in the geomagnetic field. Panel (a) shows the helium flux measured in this experiment as a function of rigidity; Panel (b) shows the fitted transmission function as resulting from the ratio of the experimental points and the normalized curve given in Fig. 13 for maximum solar modulation.

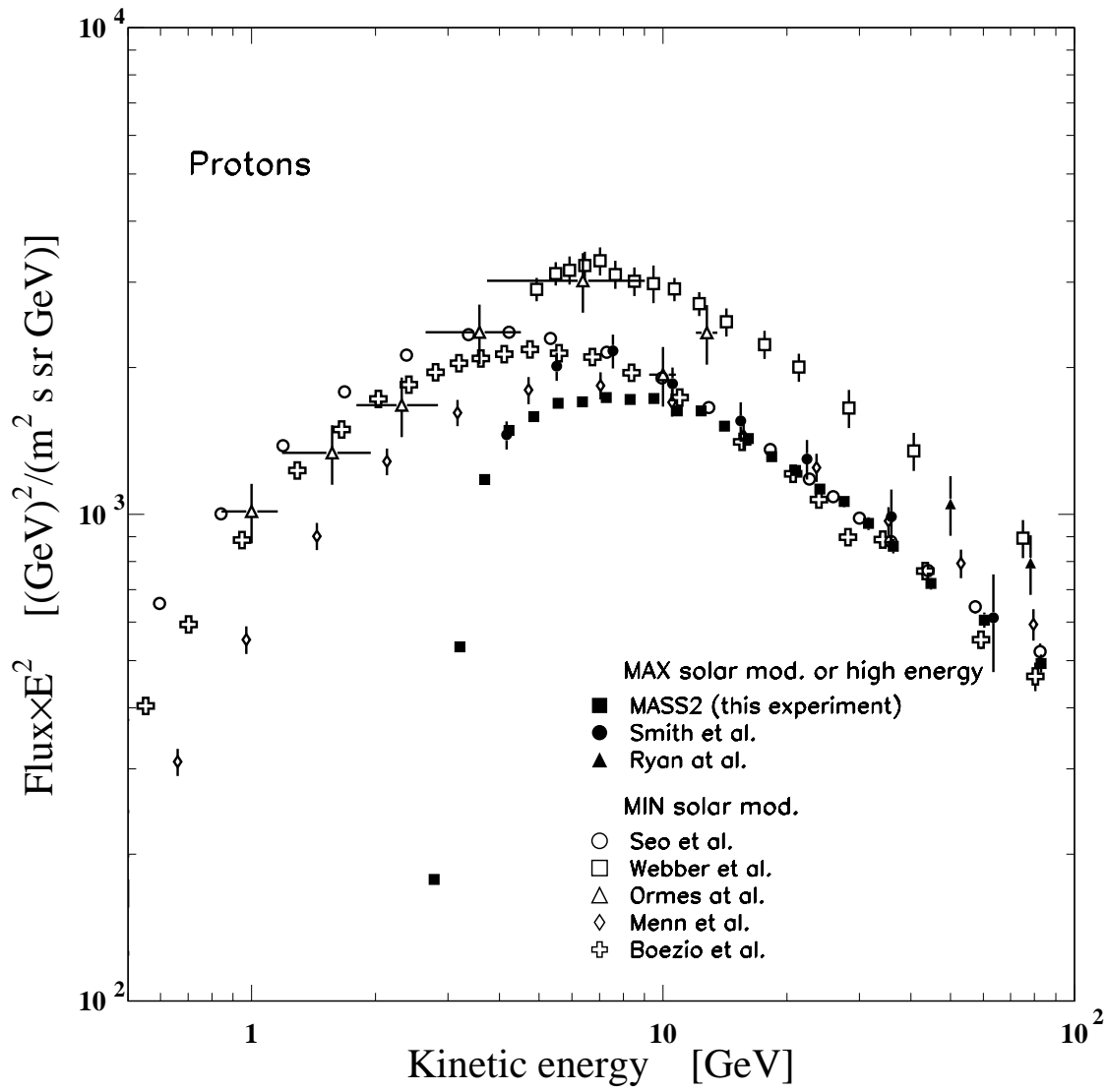


FIG. 15. Comparison between the proton flux measured in this experiment and other data: Smith *et al.* [45], Ryan *et al.* [46], Seo *et al.* [47], Webber *et al.* [48], Ormes *et al.* [49], Menn *et al.* [50], Boezio *et al.* [51].

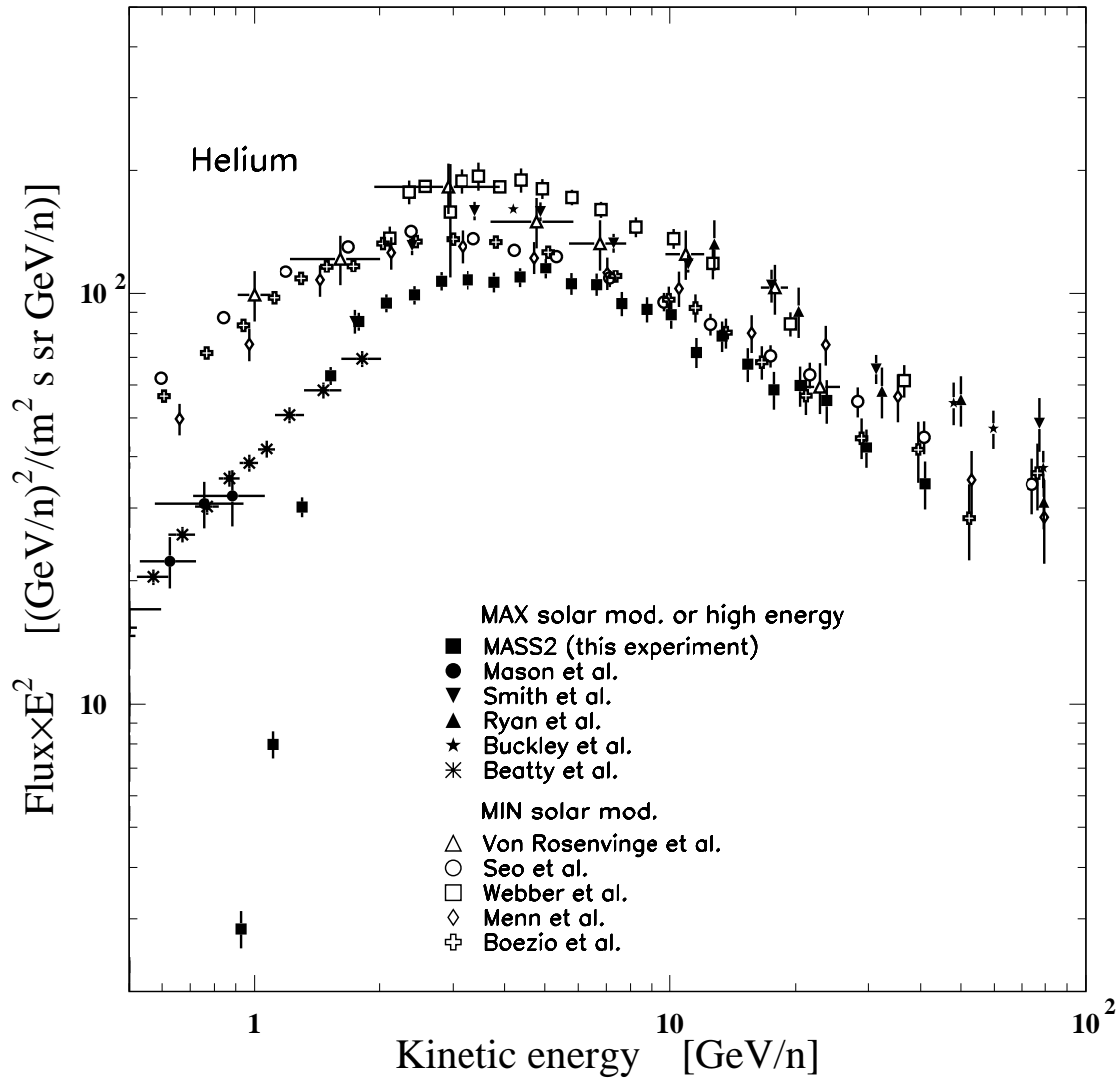


FIG. 16. Comparison between the helium flux measured in this experiment and other data: Smith *et al.* [45], Ryan *et al.* [46], Seo *et al.* [47], Webber *et al.* [48], Menn *et al.* [50], Boezio *et al.* [51], Mason *et al.* [52], Von Rosenvinge *et al.* [53], Buckley *et al.* [54], Beatty *et al.* [55].

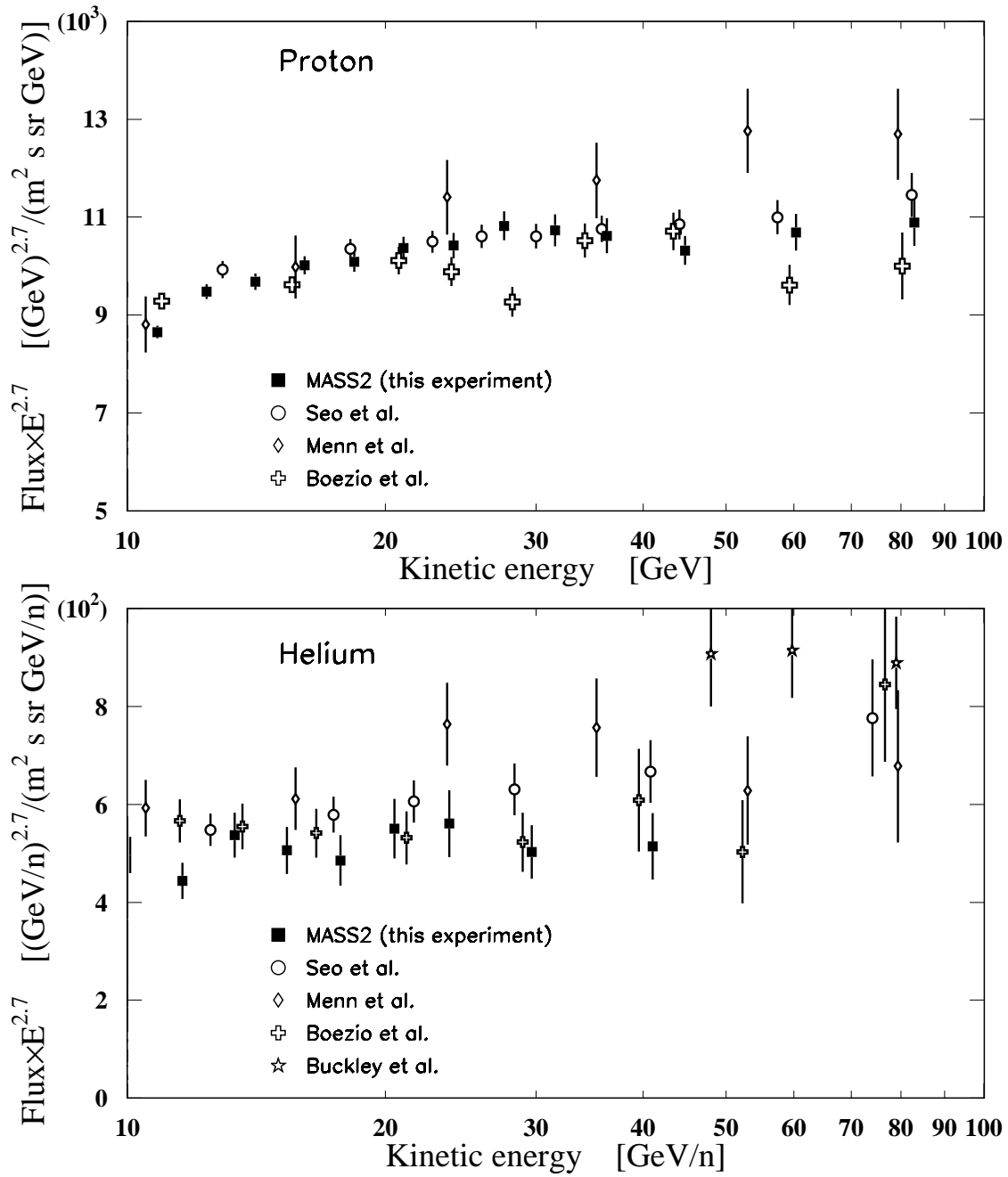


FIG. 17. Comparison of the most recent high-energy measurements of proton and helium fluxes: Seo *et al.* [47], Menn *et al.* [50], Boezio *et al.* [51], Buckley *et al.* [54].

TABLE I. Selection criteria for track reconstruction

Test	Description
1	at least 11 signals in the spectrometer along the x -view ^a
2	at least 8 signals in the spectrometer along the y -view ^a
3	not more than 3 multiple hits, ^b x -view ^a
4	not more than 3 multiple hits, ^b y -view ^a
5	$\chi_x^2 \leq 8$ and $\chi_y^2 \leq 8$
6	the reconstructed deflection uncertainty $\sigma_n \leq 0.03 \text{ GV}^{-1}$
7	extrapolated track and positions in the scintillators ^c consistent within 10 cm
8	reconstructed track crossing the calorimeter
9	extrapolation of the track not intersecting the lift bar
10	β , as measured from the T.O.F., between 0 and 2

^aThe x -view is the maximum curvature axis, the y -view the perpendicular direction.

^bMultiple hits were defined as signals in the drift chambers at a distance larger than 4 cm from the reconstructed track.

^cThe crossing positions in the scintillators were estimated by using the time signals from the T.O.F. system.

TABLE II. Selection criteria for muons

Test	Description
1	pulse height from the top scintillators ^a between 0.7 and $1.8 I_0$
2	number of x -view hits in the calorimeter between 2 and 10
3	number of y -view hits in the calorimeter between 2 and 14
4	not more than 1 multiple calorimeter hits along each view
5	Cherenkov signal less than the equivalent to 3 photoelectrons at less than 0.8 GV
6	squared mass ^b $m^2 \leq 0.5 \text{ GeV}^2$ in the rigidity range 0.65–1.25 GV
	squared mass ^b $m^2 \leq 0.3 \text{ GeV}^2$ in the rigidity range 1.25–1.5 GV

^aas determined from (3.1).

^bas from equation (3.4).

TABLE III. Sources for muon background

source	Rejection criteria	Residual contamination
albedo ^a	T.O.F. measurement	none
low-energy electrons and positrons ^b	Cherenkov test	$\lesssim 1\%$ below 0.5 GV
spillover protons ^a	no correction	negligible
atmospheric mesons ^b	no correction	$\lesssim 1\text{-}2\%$ almost everywhere for $\lesssim 10 \text{ GeV}/c$ pions; negligible for kaons
locally-produced mesons ^b	track reconstruction requirements	$\lesssim 5\%$ above 50 g/cm ² below 1 GeV/ c ; negligible above 1 GeV/ c
low-energy protons ^c	T.O.F. measurement	$\lesssim 1\%$

^aFor μ^- .

^bBoth for μ^+ and μ^- .

^cFor μ^+ .

TABLE IV. Flux growth curve results for 0.3–40 GeV/ c negative and 0.3–1.5 GeV/ c positive muons. Results are given for the following momentum intervals: I 0.3–0.9 GeV/ c , II 0.9–1.5 GeV/ c , III 1.5–2.5 GeV/ c , IV 2.5–4 GeV/ c , V 4–40 GeV/ c . The symbols APD and FAD stand respectively for Average Payload Depth and Flux-weighted Average Depth in the momentum bin. In the latter case, the best fit curve of type (4.1) was used. The units of flux are particles/($\text{cm}^2 \text{ s sr GeV}/c$).

Depth Interval		A	B	C	D
Duration (s)		820	530	350	390
Live-time fraction		0.920	0.818	0.725	0.648
Initial depth (g/cm^2)		886	514	358	272
Final depth (g/cm^2)		514	358	272	197
APD (g/cm^2)		680	434	316	233
I	μ^- Flux	$2.59 \pm 0.28 \cdot 10^{-3}$	$6.49 \pm 0.59 \cdot 10^{-3}$	$9.79 \pm 0.95 \cdot 10^{-3}$	$1.03 \pm 0.10 \cdot 10^{-2}$
	FAD (g/cm^2)	631.6	421.3	309.1	228.7
II	μ^- Flux	$2.25 \pm 0.24 \cdot 10^{-3}$	$4.21 \pm 0.43 \cdot 10^{-3}$	$5.87 \pm 0.66 \cdot 10^{-3}$	$6.33 \pm 0.69 \cdot 10^{-3}$
	FAD (g/cm^2)	637.4	422.6	309.5	229.0
III	μ^- Flux	$1.24 \pm 0.14 \cdot 10^{-3}$	$2.13 \pm 0.23 \cdot 10^{-3}$	$2.70 \pm 0.34 \cdot 10^{-3}$	$3.44 \pm 0.39 \cdot 10^{-3}$
	FAD (g/cm^2)	639.5	423.0	309.7	229.1
IV	μ^- Flux	$5.30 \pm 0.71 \cdot 10^{-4}$	$8.89 \pm 1.22 \cdot 10^{-4}$	$1.10 \pm 0.18 \cdot 10^{-3}$	$1.24 \pm 0.19 \cdot 10^{-3}$
	FAD (g/cm^2)	645.0	424.2	310.0	229.4
V	μ^- Flux	$4.25 \pm 0.41 \cdot 10^{-5}$	$5.36 \pm 0.61 \cdot 10^{-5}$	$6.49 \pm 0.87 \cdot 10^{-5}$	$5.82 \pm 0.83 \cdot 10^{-5}$
	FAD (g/cm^2)	650.3	425.3	310.4	229.6
I	μ^+ Flux	$2.84 \pm 0.29 \cdot 10^{-3}$	$6.99 \pm 0.62 \cdot 10^{-3}$	$9.30 \pm 0.92 \cdot 10^{-3}$	$1.30 \pm 0.11 \cdot 10^{-2}$
	FAD (g/cm^2)	630.5	421.1	309.0	228.6
II	μ^+ Flux	$2.92 \pm 0.28 \cdot 10^{-3}$	$4.85 \pm 0.47 \cdot 10^{-3}$	$6.80 \pm 0.72 \cdot 10^{-3}$	$7.79 \pm 0.77 \cdot 10^{-3}$
	FAD (g/cm^2)	637.2	422.6	309.5	229.0

TABLE IV. (continued)

Depth Interval		E	F	G	H
Duration (s)		510	670	670	780
Live-time fraction		0.594	0.597	0.593	0.602
Initial depth (g/cm^2)		197	134	95	69
Final depth (g/cm^2)		134	95	69	48
APD (g/cm^2)		163	112	81	59
I	μ^- Flux	$1.16 \pm 0.10 \cdot 10^{-2}$	$9.93 \pm 0.78 \cdot 10^{-3}$	$8.85 \pm 0.74 \cdot 10^{-3}$	$7.64 \pm 0.63 \cdot 10^{-3}$
	FAD (g/cm^2)	160.4	110.5	80.4	58.2
II	μ^- Flux	$6.09 \pm 0.64 \cdot 10^{-3}$	$6.11 \pm 0.54 \cdot 10^{-3}$	$5.35 \pm 0.51 \cdot 10^{-3}$	$4.17 \pm 0.41 \cdot 10^{-3}$
	FAD (g/cm^2)	160.6	110.6	80.4	58.2
III	μ^- Flux	$3.23 \pm 0.34 \cdot 10^{-3}$	$2.80 \pm 0.28 \cdot 10^{-3}$	$2.57 \pm 0.27 \cdot 10^{-3}$	$1.90 \pm 0.21 \cdot 10^{-3}$
	FAD (g/cm^2)	160.7	110.6	80.5	58.2
IV	μ^- Flux	$1.32 \pm 0.18 \cdot 10^{-3}$	$9.29 \pm 1.30 \cdot 10^{-4}$	$8.45 \pm 1.24 \cdot 10^{-4}$	$6.54 \pm 1.00 \cdot 10^{-4}$
	FAD (g/cm^2)	160.9	110.7	80.5	58.2
V	μ^- Flux	$4.95 \pm 0.70 \cdot 10^{-5}$	$4.71 \pm 0.59 \cdot 10^{-5}$	$3.78 \pm 0.53 \cdot 10^{-5}$	$3.01 \pm 0.44 \cdot 10^{-5}$
	FAD (g/cm^2)	161.1	110.8	80.5	58.2
I	μ^+ Flux	$1.29 \pm 0.10 \cdot 10^{-2}$	$1.16 \pm 0.08 \cdot 10^{-2}$	$9.71 \pm 0.77 \cdot 10^{-3}$	$8.56 \pm 0.66 \cdot 10^{-3}$
	FAD (g/cm^2)	160.4	110.5	80.4	58.2
II	μ^+ Flux	$8.46 \pm 0.69 \cdot 10^{-3}$	$7.54 \pm 0.61 \cdot 10^{-3}$	$5.54 \pm 0.52 \cdot 10^{-3}$	$4.41 \pm 0.43 \cdot 10^{-3}$
	FAD (g/cm^2)	160.6	110.6	80.4	58.2

TABLE IV. (continued)

Depth Interval		I	J
Duration (s)		1100	3590
Live-time fraction		0.619	0.646
Initial depth (g/cm ²)		48	27
Final depth (g/cm ²)		27	5
APD (g/cm ²)		37	13
I	μ^- Flux	$4.78 \pm 0.41 \cdot 10^{-3}$	$2.00 \pm 0.14 \cdot 10^{-3}$
	FAD (g/cm ²)	37.4	15.3
II	μ^- Flux	$2.44 \pm 0.26 \cdot 10^{-3}$	$1.02 \pm 0.09 \cdot 10^{-3}$
	FAD (g/cm ²)	37.4	15.3
III	μ^- Flux	$1.29 \pm 0.14 \cdot 10^{-3}$	$5.11 \pm 0.50 \cdot 10^{-4}$
	FAD (g/cm ²)	37.4	15.3
IV	μ^- Flux	$4.20 \pm 0.67 \cdot 10^{-4}$	$1.60 \pm 0.22 \cdot 10^{-4}$
	FAD (g/cm ²)	37.4	15.4
V	μ^- Flux	$2.50 \pm 0.33 \cdot 10^{-5}$	$9.63 \pm 1.12 \cdot 10^{-6}$
	FAD (g/cm ²)	37.4	15.4
I	μ^+ Flux	$5.57 \pm 0.45 \cdot 10^{-3}$	$2.38 \pm 0.16 \cdot 10^{-3}$
	FAD (g/cm ²)	37.4	15.3
II	μ^+ Flux	$3.08 \pm 0.30 \cdot 10^{-3}$	$1.41 \pm 0.11 \cdot 10^{-3}$
	FAD (g/cm ²)	37.4	15.3

TABLE V. Negative muon spectra in different depth intervals. The results are given for the following momentum bins: I 0.3–0.465 GeV/c, II 0.465–0.65 GeV/c, III 0.65–0.8 GeV/c, IV 0.8–1 GeV/c, V 1–1.25 GeV/c, VI 1.25–1.5 GeV/c, VII 1.5–2 GeV/c, VIII 2–3 GeV/c, IX 3–8 GeV/c, X 8–40 GeV/c. The symbols APD and FAD stand respectively for Average Payload Depth and Flux-weighted Average Depth in the momentum bin. In the latter case, the best fit curve of type (4.1) was used. The units of flux are particles/(cm² s sr GeV/c).

Depth Interval		A	B	C	D	E
Duration (s)		540	700	510	1190	1230
Live-time fraction		0.627	0.594	0.592	0.600	0.620
Initial depth (g/cm ²)		255	164	106	83	48
Final depth (g/cm ²)		164	106	83	48	25
APD (g/cm ²)		206	131	94	65	36
FAD (g/cm ²)		202	130	93	65	36
I	μ^- Flux	$1.21 \pm 0.20 \cdot 10^{-2}$	$1.48 \pm 0.20 \cdot 10^{-2}$	$1.16 \pm 0.20 \cdot 10^{-2}$	$1.06 \pm 0.12 \cdot 10^{-2}$	$5.58 \pm 0.88 \cdot 10^{-3}$
II	μ^- Flux	$1.06 \pm 0.15 \cdot 10^{-2}$	$1.22 \pm 0.14 \cdot 10^{-2}$	$8.58 \pm 1.42 \cdot 10^{-3}$	$7.96 \pm 0.90 \cdot 10^{-3}$	$5.13 \pm 0.69 \cdot 10^{-3}$
III	μ^- Flux	$9.00 \pm 1.45 \cdot 10^{-3}$	$9.46 \pm 1.35 \cdot 10^{-3}$	$7.78 \pm 1.43 \cdot 10^{-3}$	$6.63 \pm 0.86 \cdot 10^{-3}$	$4.18 \pm 0.66 \cdot 10^{-3}$
IV	μ^- Flux	$8.41 \pm 1.20 \cdot 10^{-3}$	$7.82 \pm 1.04 \cdot 10^{-3}$	$6.98 \pm 1.15 \cdot 10^{-3}$	$6.47 \pm 0.73 \cdot 10^{-3}$	$3.29 \pm 0.50 \cdot 10^{-3}$
V	μ^- Flux	$6.09 \pm 0.90 \cdot 10^{-3}$	$6.91 \pm 0.87 \cdot 10^{-3}$	$6.39 \pm 0.98 \cdot 10^{-3}$	$4.90 \pm 0.56 \cdot 10^{-3}$	$2.76 \pm 0.40 \cdot 10^{-3}$
VI	μ^- Flux	$4.83 \pm 0.80 \cdot 10^{-3}$	$4.90 \pm 0.73 \cdot 10^{-3}$	$4.69 \pm 0.83 \cdot 10^{-3}$	$3.29 \pm 0.45 \cdot 10^{-3}$	$1.86 \pm 0.33 \cdot 10^{-3}$
VII	μ^- Flux	$4.13 \pm 0.52 \cdot 10^{-3}$	$3.31 \pm 0.42 \cdot 10^{-3}$	$3.55 \pm 0.51 \cdot 10^{-3}$	$2.73 \pm 0.29 \cdot 10^{-3}$	$1.60 \pm 0.22 \cdot 10^{-3}$
VIII	μ^- Flux	$2.58 \pm 0.29 \cdot 10^{-3}$	$2.18 \pm 0.24 \cdot 10^{-3}$	$1.43 \pm 0.23 \cdot 10^{-3}$	$1.30 \pm 0.14 \cdot 10^{-3}$	$7.21 \pm 1.02 \cdot 10^{-4}$
IX	μ^- Flux	$4.79 \pm 0.56 \cdot 10^{-4}$	$2.97 \pm 0.39 \cdot 10^{-4}$	$4.02 \pm 0.54 \cdot 10^{-4}$	$2.39 \pm 0.27 \cdot 10^{-4}$	$1.96 \pm 0.24 \cdot 10^{-4}$
X	μ^- Flux	$2.44 \pm 0.49 \cdot 10^{-5}$	$2.30 \pm 0.43 \cdot 10^{-5}$	$1.64 \pm 0.42 \cdot 10^{-5}$	$1.43 \pm 0.26 \cdot 10^{-5}$	$8.66 \pm 1.94 \cdot 10^{-6}$

TABLE VI. Proton flux at the top of the atmosphere.

Kin. energy range (GeV)		mean energy (GeV)	flux	flux error $(\text{m}^2 \text{ sr s GeV})^{-1}$
2.55	2.95	2.77	23.10	0.48
2.95	3.41	3.21	51.84	0.71
3.41	3.93	3.68	86.90	0.92
3.93	4.52	4.22	83.46	0.85
4.52	5.19	4.85	67.66	0.72
5.19	5.95	5.56	54.80	0.60
5.95	6.81	6.36	42.04	0.48
6.81	7.78	7.28	32.83	0.40
7.78	8.89	8.31	24.90	0.32
8.89	10.1	9.49	19.18	0.26
10.1	11.6	10.8	13.90	0.21
11.6	13.2	12.3	10.66	0.17
13.2	15.1	14.1	7.63	0.13
15.1	17.2	16.1	5.52	0.10
17.2	19.7	18.3	3.89	0.08
19.7	22.5	21.0	2.79	0.06
22.5	25.7	24.0	1.95	0.05
25.7	29.5	27.5	1.40	0.04
29.5	33.9	31.6	0.961	0.029
33.9	39.0	36.3	0.652	0.022
39.0	52.2	44.8	0.360	0.010
52.2	71.0	60.3	0.167	0.006
71.0	99.1	83.0	0.072	0.003

TABLE VII. Helium flux at the top of the atmosphere.

Kin. energy range (GeV/n)		mean energy (GeV/n)	flux	flux error $(\text{m}^2 \text{ sr s GeV/n})^{-1}$
.841	1.00	.927	3.30	.34
1.00	1.19	1.11	6.53	.49
1.19	1.40	1.30	17.7	1.0
1.40	1.64	1.52	27.2	1.4
1.64	1.92	1.78	27.0	1.3
1.92	2.24	2.08	21.9	1.1
2.24	2.62	2.42	16.9	0.9
2.62	3.03	2.82	13.5	0.7
3.03	3.51	3.26	10.1	0.5
3.51	4.06	3.77	7.48	0.41
4.06	4.68	4.36	5.78	0.32
4.68	5.39	5.02	4.58	0.26
5.39	6.20	5.77	3.17	0.19
6.20	7.13	6.64	2.38	0.15
7.13	8.20	7.63	1.62	0.11
8.20	9.42	8.77	1.19	0.08
9.42	10.8	10.1	0.875	0.065
10.8	12.4	11.6	0.536	0.045
12.4	14.3	13.3	0.444	0.038
14.3	16.5	15.3	0.286	0.027
16.5	19.1	17.7	0.186	0.020
19.1	22.1	20.5	0.142	0.016
22.1	25.7	23.7	0.098	0.011
25.7	35.0	29.7	0.048	0.005
35.0	49.1	41.0	0.020	0.0027